RESEARCH ARTICLE

Intraflagellar transport protein IFT172 contains a C-terminal ubiquitin-binding U-box-like domain involved in ciliary signaling

Nevin K Zacharia[1], Stefanie Kuhns[2], Niels Boegholm[1], Anni Christensen[1], Jiaolong Wang[1], Narcis A Petriman[1,3], Anna Lorentzen[1], Jindriska L Fialova[3], Lucie Menguy[4], Sophie Saunier[4], Søren Tvorup Christensen[3], Jens S Andersen[2], Sagar Bhogaraju[5]*, Esben Lorentzen[1]*

[1]Department of Molecular Biology and Genetics, Aarhus University, Aarhus, Denmark; [2]Department for Biochemistry and Molecular Biology, University of Southern Denmark, Odense, Denmark; [3]Department of Biology, University of Copenhagen, Universitetsparken, Copenhagen Ø, Denmark; [4]Laboratory of Hereditary and Kidney diseases, Institut Imagine, Paris, France; [5]European Molecular Biology Laboratory, Grenoble, France

***For correspondence:** bhogaraju@embl.fr (SB); el@mbg.au.dk (EL)

Competing interest: The authors declare that no competing interests exist.

Funding: See page 23

Preprint posted 05 November 2024
Sent for Review 13 November 2024
Reviewed preprint posted 31 January 2025
Reviewed preprint revised 06 May 2026
Version of Record 23 June 2026

Reviewing Editor: Junmin Pan, Tsinghua University, China

© Copyright Zacharia *et al*. This article is distributed under the terms of the Creative Commons Attribution License, which permits unrestricted use and redistribution provided that the original author and source are credited.

eLife Assessment

This **important** work advances our understanding of intraflagellar transport, ciliogenesis, and ciliary-based signaling, by identifying the interactions of IFT172 with IFT-A components, ubiquitin-binding, and ubiquitination, mediated by IFT172 C-terminus and its role in ciliogenesis and ciliary signaling. The evidence supporting the findings is **convincing**. This paper will be of interest to cell biologists and biochemists, especially those working on cilia and signaling.

Abstract Intraflagellar transport (IFT) is a fundamental process driving ciliogenesis in most eukaryotic organisms. IFT172, the largest protein of the IFT complex, plays a crucial role in cilium formation, and several disease-causing IFT172 variants have been identified in ciliopathy patients. While IFT172 is tethered to the IFT-B complex via its N-terminal domains, the function of its C-terminal domains has remained elusive. Here, using both human and *Chlamydomonas reinhardtii* IFT172, we reveal that the C-terminal part of IFT172 interacts with IFT-A complex subunits, providing a molecular basis for the role of IFT172 in bridging IFT-A and IFT-B complexes. We determine the crystal structure of the C-terminal part of IFT172, uncovering a conserved U-box-like domain often found in E3 ubiquitin ligases. This domain exhibits ubiquitin-binding properties, and IFT172 undergoes ubiquitin conjugation in vitro, an activity that is reduced in the C1727R patient ciliopathy variant. We use CRISPR-engineered RPE-1 cells to demonstrate that the U-box-like domain is essential for IFT172 protein stability and proper cilium formation. Notably, RPE-1 cells with heterozygous deletion of the U-box domain show altered TGF-β signaling responses, particularly in SMAD2 phosphorylation levels and AKT activation. Our findings suggest that IFT172, beyond its structural role in bridging IFT-A and IFT-B complexes within IFT trains, harbors a conserved U-box-like domain with potential involvement in ciliary ubiquitination processes and signaling, providing new insights into the molecular mechanisms underlying IFT172-related ciliopathies.

Introduction

Cilia are hair-like microtubule (MT)-based organelles that protrude from the cell surface of vertebrate cells and in several eukaryotic single-celled organisms. Cilia play indispensable roles in cellular motility, extracellular fluid flow, sensing extracellular cues, and coordinating cellular signaling pathways (**Satir and Christensen, 2007**). They are highly conserved from unicellular eukaryotes to humans and can vary greatly in length, copy number, and function. For example, in the unicellular algae *Chlamydomonas reinhardtii* (Cr), beating motions generated by motile cilia propel the cells through media (**Wan, 2018**). Additionally, most vertebrate cells possess a single copy of non-motile primary cilia that perform sensory and signaling functions. The sensory capabilities of the primary cilium are attributed to ciliary coordination of signaling pathways such as transforming growth factor β (TGF-β)/bone morphogenetic protein (BMP), platelet-derived growth factor (PDGF), and Hedgehog to drive organismal development and tissue homeostasis (**Mill et al., 2023**). Aberrations to cilium assembly or function lead to a class of human genetic disorders termed ciliopathies (**Reiter and Leroux, 2017**). Ciliopathies affect a wide range of organs, including the liver, kidney, and skeletal system, and often manifest as syndromes such as Bardet-Biedl syndrome and Meckel-Gruber syndrome with overlapping phenotypes (**Focșa et al., 2021**).

The proper assembly and function of cilia require a bidirectional trafficking system known as intraflagellar transport (IFT; **Rosenbaum and Witman, 2002**; **Kozminski et al., 1993**; **Kozminski et al., 1995**) to shuttle key ciliary components (**Bhogaraju et al., 2014**; **Lechtreck, 2015**), including membrane-bound receptors such as G-protein-coupled receptors (GPCRs) and ion channels that mediate signaling and sensory responses, between the cilium organelle and the cytoplasm (**Lechtreck, 2015**; **Long and Huang, 2020**; **Mukhopadhyay et al., 2010**). IFT is carried out by the 23 subunit IFT complex that polymerizes into IFT trains (**Kozminski et al., 1995**; **Pigino et al., 2009**) and traverses along the ciliary MT axoneme. IFT trains assemble at the ciliary base (**van den Hoek et al., 2022**), associate with ciliary cargo (**Lechtreck, 2015**; **Taschner and Lorentzen, 2016**), and undergo anterograde transport from the ciliary base to the tip powered by the Kinesin-2 motor (**Kozminski et al., 1995**; **Wingfield et al., 2017**). A major remodeling of the anterograde IFT trains occurs at the ciliary tip (**Pedersen et al., 2006**), forming retrograde IFT trains that have a distinct ultrastructure (**Jordan et al., 2018**), which subsequently traverse from the tip to the ciliary base powered by the Dynein-2 motor (**Pazour et al., 1999**; **Porter et al., 1999**). The IFT complex associates with the octameric BBSome complex to facilitate the targeted ciliary exit of several proteins (**Eguether et al., 2014**; **Nachury et al., 2007**). The IFT trains are primarily understood to function as adaptors between the molecular motors and ciliary cargo to facilitate the dynamic localization of signaling components.

Ubiquitination is a well-studied posttranslational modification (**Komander and Rape, 2012**) that was recently shown to be crucial in ciliary homeostasis (**Hossain and Tsang, 2019**; **Lv et al., 2021**; **Shinde et al., 2020**). Ubiquitination is a multi-step enzymatic cascade where a ubiquitin molecule is shuttled from an E1 enzyme to the E2 enzyme and finally transferred to the substrate protein mediated by an E3 ligase (**Komander and Rape, 2012**). Ubiquitination is known to be important in flagella disassembly in *Cr* (**Huang et al., 2009**). Upon initiation of flagellar resorption, there is an upregulation of ubiquitination events, specifically that of tubulin subunits, facilitating ciliary disassembly (**Huang et al., 2009**; **Wang et al., 2019**). Ubiquitination is also critical to ciliary signaling. The ciliary Hedgehog signaling pathway is a well-studied example of how regulatory ubiquitination events control signal-dependent repression and activation of ciliary signaling (**Lv et al., 2021**; **Shinde et al., 2020**; **Desai et al., 2020**; **Kim et al., 2015**). In the absence of the Sonic Hedgehog ligand (SHH), the ciliary levels of the signal-transducing protein smoothened (SMO) are kept low for pathway repression (**Desai et al., 2020**). This is achieved by the ubiquitination of SMO by the ciliary localized ubiquitin ligase WWP1, an event that subsequently targets SMO for IFT-dependent ciliary exit (**Lv et al., 2021**; **Desai et al., 2020**). Upon SHH binding, the ciliary exit of the ligand-bound PTCH1 receptor and negative pathway regulator GPR161 occurs by the targeted ubiquitination of these receptors (**Shinde et al., 2020**; **Kim et al., 2015**), leading to pathway activation. In the case of several GPCRs, such as GPR161 and SSTR3, signal-dependent ciliary exit specifically relies on the ubiquitination of these receptors and subsequent IFT-dependent ciliary exit (**Shinde et al., 2020**). *Bona fide* ubiquitin recognition domains are yet to be identified in the IFT complex. Instead, the BBSome complex was shown to facilitate the recognition of these ubiquitinated GPCRs mediated by the TOM1L2 adaptor protein that harbors VHS and GAT domains capable of ubiquitin binding (**Shinde et al., 2023**). Moreover, a recent analysis of

ubiquitinated proteins in the cilium of RPE1 cells identified signaling-related proteins to be enriched in the data set (***Aslanyan et al., 2023***). Specifically, components of the Wnt, Notch, and TGF-β pathway were identified as targets of ciliary ubiquitination events. The BBSome complex, which mediates signal-dependent ciliary exit of a wide array of ubiquitinated GPCRs, is in turn dependent on ubiquitination for proper assembly and function (***Chiuso et al., 2023***). The cilium-associated ubiquitin ligase PJA2 ubiquitinates the BBSome subunits BBS1 and BBS4, which are essential for normal BBSome assembly and ciliary GPCR trafficking (***Chiuso et al., 2023***). Cilium-associated ubiquitin ligases and ubiquitin-binding domains (UBDs) thus emerge as crucial players in maintaining ciliary homeostasis.

IFT172 is the largest subunit in the IFT complex and is part of the IFT-B2 subcomplex (***Taschner et al., 2016***). The WD40 repeat containing N-terminal domain of the protein mediates interaction with the subunits IFT57 and IFT80, thereby maintaining IFT172 association with the IFT-B complex (***Taschner et al., 2016***; ***Petriman et al., 2022***). The C-terminal tetratricopeptide repeats (TPRs) of IFT172 remain rather uncharacterized in terms of structure and function despite the fact that IFT172 C-terminal variants have been detected in a cohort of ciliopathy patients with severe skeletal ciliopathy syndromes (Jeune syndrome and Mainzer-Saldino syndrome; ***Halbritter et al., 2013***). Another cohort of patients with phenotypically slightly different ciliopathy features resembling BBS also presented with IFT172 variations predominantly resulting in retinal defects (***Bujakowska et al., 2015***). Lastly, an isolated case of a patient exhibiting growth retardation was reported to have compound heterozygous IFT172 C-terminal mutations (***Lucas-Herald et al., 2015***). The importance of the IFT172 C-terminus is further exemplified by prior studies on various in vivo models. IFT172^{wim} mice carry a C-terminal point mutation (L1564P) causing major developmental defects and embryonic lethality caused by a complete loss of cilium in the embryonic node (***Huangfu et al., 2003***). The *C. reinhardtii* strain *fla11* carries the point mutation L1615P at the C-terminal TPRs of IFT172 resulting in flagellar resorption and IFT particle accumulation at the ciliary tip of green algae (***Pedersen et al., 2005***), a phenotype that was recapitulated in *Tetrahymena thermophila* models having progressive IFT172 C-terminal deletions (***Tsao and Gorovsky, 2008***). Furthermore, it was observed that the *C. reinhardtii fla11* strain accumulates ubiquitinated proteins in the cilium (***Williamson et al., 2012***), which suggests that IFT172 could be involved in ciliary ubiquitination events. However, the molecular bases for these observations are currently not known.

In this study, we focused on structural and functional characterization of the IFT172 C-terminal region to reveal an interaction with IFT-A components and a C-terminal ubiquitin-binding U-box domain that may be involved in ciliary ubiquitination and signaling pathways.

Results

IFT172$_{968\text{-}C}$ interacts directly with subunits of the IFT-A complex

While the N-terminal β-propeller of CrIFT172 interacts with CrIFT57 and a central region (residues 626–785) interacts with CrIFT80, little is known about the function of the C-terminal 800 residues of IFT172. This region is predicted to fold into 20 TPRs followed by a small 70–80 residue domain of unknown function (***Figure 1A***).

We purified the C-terminal fragment of IFT172 protein (His-tagged CrIFT172$_{968\text{-}C}$) to homogeneity (***Figure 1—figure supplement 1A***) and carried out pull-down assays from an extract of isolated *C. reinhardtii* cilia (***Figure 1—figure supplement 1B***). His-tagged Tobacco Etch Virus (TEV) protein was used as a negative control when detecting CrIFT172$_{968\text{-}C}$ interactors by mass spectrometry (MS; ***Figure 1—figure supplement 1C and D***). Based on the resulting volcano plot (***Figure 1—figure supplement 1C***, see also Materials and methods), 10 proteins were annotated as interactors of CrIFT172$_{968\text{-}C}$ (***Figure 1—figure supplement 1D***). Consistent with the fact that the CrIFT172$_{968\text{-}C}$ construct does not contain the IFT-B complex associating domains, no IFT-B proteins were found as interactors (***Figure 1—figure supplement 1D***). Interestingly, however, several components of the IFT-A complex were identified as interaction partners of CrIFT172$_{968\text{-}C}$ including IFT144, IFT140, and IFT139. Furthermore, a CH-domain containing protein of the central apparatus of the cilium as well as six additional proteins without a published ciliary localization were identified as IFT172 interactors (***Figure 1—figure supplement 1D***).

To assess which of the 10 significant hits are direct interaction partners of CrIFT172$_{968\text{-}C}$, structural modeling using AlphaFold multimer (AF-M) (***Jumper et al., 2021***; ***Evans, 2021***) was carried

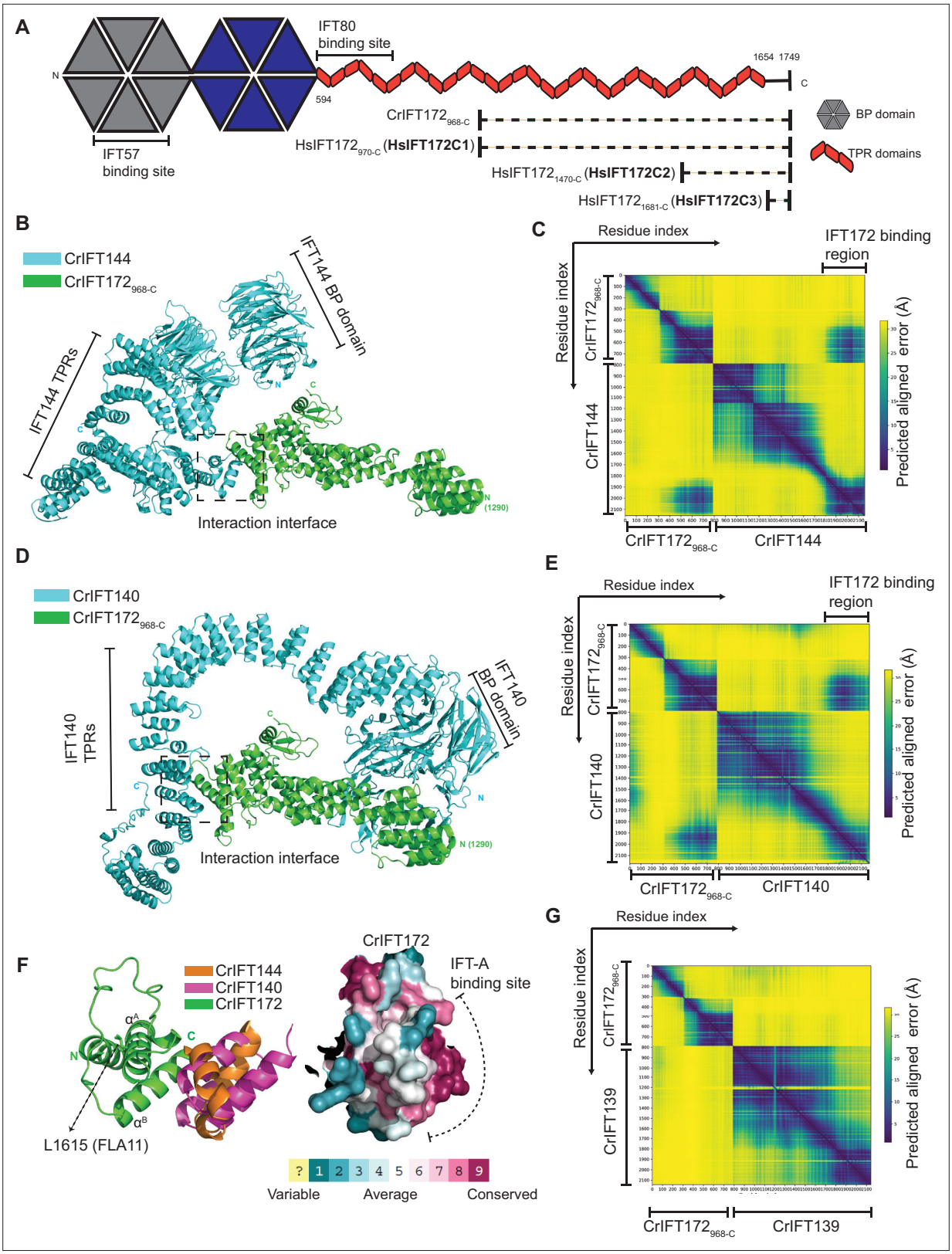


Figure 1. The C-terminal TPRs of IFT172 constitute a binding site for IFT-A subunits. (**A**) Schematic representation of *Homo sapiens* (Hs) IFT172 protein domain organization. β-propeller and TPR (tetratricopeptide repeat) domains are indicated. Solid lines represent previously identified IFT57 and IFT80 binding sites. Dashed lines show various truncated constructs of *Chlamydomonas reinhardtii* (Cr) IFT172 and HsIFT172 used in this study. (**B**) Cartoon representation of the AlphaFold predicted structural model for a complex between $CrIFT172_{968\text{-}C}$ and CrIFT144. The interaction interface is highlighted.

Figure 1 continued on next page

Figure 1 continued

(**C**) Predicted Aligned Error (PAE) plot for the AlphaFold model in panel B. X- and Y-axes show indexed residues from each protein used for PAE calculation. Low PAE scores indicate high confidence in the predicted interaction interface. (**D**) Cartoon representation of the AlphaFold predicted structural model for a complex between CrIFT172$_{968\text{-}C}$ and CrIFT140, highlighting the interaction interface. (**E**) PAE plot for the AlphaFold model in panel D, showing high confidence (low PAE values) for the interaction interface residue pairs. (**F**) Left: Structural superposition of interaction interfaces from AlphaFold models in panels B and D. Subunits are colored as indicated. IFT144 and IFT140 are predicted to associate with an identical binding site formed by IFT172 TPR helices αA and αB. The L1615P temperature-sensitive mutation identified in the *fla11* strain of *C. reinhardtii* maps onto helix αA. Right: Surface amino acid conservation map for the IFT144/140 binding site in IFT172, color-coded as indicated. (**G**) PAE plot for an AlphaFold predicted structure of the CrIFT172$_{968\text{-}C}$-CrIFT139 complex. High PAE scores for all inter-chain residue pairs suggest that IFT172 and IFT139 do not interact directly.

The online version of this article includes the following source data and figure supplement(s) for figure 1:

Figure supplement 1. Uncovering interactors of the CrIFT172 C-terminus.

Figure supplement 1—source data 1. Uncropped, labelled Coomassie-stained SDS-PAGE gel of purified His-tagged Chlamydomonas IFT172$_{968}$–C used to generate ***Figure 1—figure supplement 1A***.

Figure supplement 1—source data 2. Original unprocessed raw image file (TIFF) of the Coomassie-stained gel shown in ***Figure 1—figure supplement 1A***.

out. This revealed three high-confidence hetero-dimeric complexes between CrIFT172$_{968\text{-}C}$ and each of the proteins: IFT144, IFT140, and a UBX-domain containing protein (uniprot: A0A2K3DQG3, CHLRE_06g293900v5; ***Figure 1B and E***, ***Figure 1—figure supplement 1E and F***). None of the other seven candidate proteins, including IFT139 (***Figure 1G***), was predicted with any confidence to interact directly with CrIFT172$_{968\text{-}C}$, and may constitute indirect interactors.

The structural model of the CrIFT172-IFT144 complex shows that the interaction is formed by the most C-terminal TPR of IFT172 (residues 1604–1669) and TPR helices of IFT144 (residues 1220–1250, see ***Figure 1B***). Surprisingly, the interaction with IFT140 (residues 1125–1162) utilizes the same TPR helices of CrIFT172 as the IFT144 interaction (***Figure 1D and F***). The structural models suggest that the interactions of IFT172 with IFT140 and IFT144 are mutually exclusive (***Figure 1F***). Both IFT172-IFT144 and IFT172-IFT140 interactions are predicted with high confidence according to the Predicted Aligned Error (PAE) plots (***Figure 1C and E***). The conservation of the IFT140 and IFT144 interaction surface on IFT172 across ciliated organisms suggests a conserved function in binding IFT-A subunits (***Figure 1F***).

We note that the IFT172 interacting helices of IFT144 are surface exposed in the cryo-EM structures of complete IFT-A complexes (***Jiang et al., 2023***) and thus free to interact with IFT172 in IFT trains. Indeed, in the published cryo-ET structures of anterograde IFT-trains in Cr, the IFT172-IFT144 complex described here is observed (***Lacey et al., 2023***). Interestingly, cryo-ET structures of retrograde IFT trains demonstrate significant rearrangements of IFT-A and B sub-complexes (***Lacey et al., 2024***) and reveal the same IFT172-IFT140 interaction as shown in ***Figure 1D–F***. The mutually exclusive interactions between IFT172 C-terminus and IFT140 or IFT144 thus underpin the different architectures of anterograde and retrograde IFT trains. ***Figure 1F*** highlights the L1615 residue, which is mutated to a proline in the *fla11* strain resulting in a retrograde IFT defect phenotype in Cr (***Pedersen et al., 2005***) and accumulation of ubiquitinated proteins (***Williamson et al., 2012***). Interestingly, the L1615 residue is located in one of the two helices of IFT172 that interact directly with IFT140 or IFT144 (annotated as helix αA in ***Figure 1F***). This L1615P mutation will disrupt the helix αA, likely resulting in impaired binding of IFT172 to the IFT-A complex. This suggests that the molecular basis for the ciliary defects observed in *fla11* is caused by impaired IFT172-IFT-A association.

The uncharacterized UBX-domain-containing protein was predicted by AF-M to be a potential direct IFT172 interactor (***Figure 1—figure supplement 1E–F***). UBX-domain-containing proteins generally function as cofactors that link the proteasome to ubiquitinated substrates, playing crucial roles in protein degradation and cellular quality control mechanisms (***Kloppsteck et al., 2012***). They often act as adaptors, facilitating recognition and processing of ubiquitinated proteins by proteasomes. The identification of a UBX-domain protein as an IFT172 interactor is consistent with previous findings demonstrating that the UBX-domain protein UBXN10 directly interacts with the IFT-B complex via CLUAP1/IFT38, recruiting the VCP/p97 ATPase to regulate IFT-B complex integrity and ciliogenesis (***Raman et al., 2015***). This suggests that UBX-domain proteins may serve broader roles as regulators of IFT complex remodeling. However, despite our interest in the interaction between IFT172 and UBX-domain-containing proteins, we could not recombinantly express the UBX-domain-containing

protein in a soluble form, which precluded further experimental characterization of its relationship with IFT172.

The crystal structure of human IFT172 reveals a C-terminal U-box-like domain

To gain deeper insights into the molecular architecture and potential functional domains of IFT172, we pursued crystallographic studies of IFT172C. Structural models of CrIFT172 predicted a small domain at the C-terminus that does not form TPRs (***Figure 2A***). This domain, which contains mixed α/β secondary structures, is linked to the IFT144 and IFT140 binding helices of IFT172 through a loop region (denoted as L0) that spans 30 residues. This arrangement places the C-terminal domain roughly 25 Å away from the IFT144 and IFT140 binding helices of IFT172 (***Figure 2A***). In our pursuit of experimental validation, we isolated and crystallized a C-terminal construct of *Homo sapiens* (Hs) $IFT172_{1470\text{-}C}$ (hereafter referred to as HsIFT172C2, see ***Figure 2—figure supplement 1A*** for purification). This construct includes the IFT144 and IFT140 binding site and the small non-TPR C-terminal domain identified in the AlphaFold model of CrIFT172 (***Figure 2A***). X-ray diffraction data were collected to 2.1 Å resolution from native crystals and 2.8 Å resolution at the peak wavelength of selenomethionine-substituted crystals (***Table 1***). Crystallographic phase information was obtained by combining molecular replacement (AlphaFold model of HsIFT172C2) and single-wavelength anomalous dispersion yielding an electron density map of excellent quality (***Figure 2—figure supplement 1B***). This map allowed for the modeling of the entire structure, excluding a small loop (residues 1656–1657) and the seven most C-terminal residues. The crystal structure reveals that HsIFT172 contains a small domain (residues 1683–1749, referred to as HsIFT172C3) at the C-terminus, which consists of a small two-stranded β-sheet followed by two α-helices (see ***Figure 2B***). The preceding TPRs and connecting loop (loop L0, colored magenta in ***Figure 2B***) pack against this C-terminal domain via a central hydrophobic core and several peripheral polar interactions (***Figure 2—figure supplement 1E***). Interestingly, numerous missense variants from ciliopathy patients (***Halbritter et al., 2013***; ***Bujakowska et al., 2015***; ***Lucas-Herald et al., 2015***) map to this interface and are highlighted in ***Figure 2B*** as yellow sticks.

Using this C-terminal HsIFT172C3 domain structure in a Distance-matrix ALIgnment (DALI; ***Holm, 2020***) search against the Protein Data Bank (PDB), structural similarities to RING domain-containing eukaryotic E3 ubiquitin ligase as well as possible prokaryotic RING domain homologues (Zinc finger proteins) were uncovered (***Figure 2—figure supplement 1C***). RING domains are among the most abundant classes of ubiquitin ligase domain in humans (***Zheng and Shabek, 2017***). Therefore, we sought to evaluate the possible structural similarity of HsIFT172C3 to various ubiquitin ligase domains. ***Figure 2C*** presents a structural comparison of the HsIFT172C3 domain with representative domains from different classes of E3 ubiquitin ligases. HsIFT172C3 superposes with RING and U-box domains with root-mean-square deviations (RMSDs) of 2.0–2.6 Å with structure-based sequence identities of 14–17% (***Figure 2C and F***). The common structural architecture of the U-box/RING domain is characterized by an N-terminal loop (L1) followed by a small two-stranded antiparallel β-sheet (β1 and β2), an α-helix (α1), and a C-terminal loop (L2; ***Figure 2C***). The RING domain fold is stabilized by the coordination of two Zn^{2+} ions, whereas the structurally and functionally similar U-box domain is instead stabilized by a network of polar contacts (***Ohi et al., 2003***; ***Aravind and Koonin, 2000***; ***Hatakeyama et al., 2001***). HsIFT172C3 has a U-box/RING domain structure with the important difference that L2 is replaced by an additional helix α2 (***Figure 2C***). Interestingly, the CrIFT172 C-terminal domain is predicted to have the L2 loop and more closely resemble canonical U-box/RING domains (***Figure 2A***). Upon inspecting the experimental electron density maps of HsIFT172C2, we did not observe any density at the corresponding Zn^{2+}-ion binding sites (see ***Figure 2D*** for an anomalous electron density map). This observation is supported by sequence alignments, which show a lack of conservation of Zn^{2+} ion coordinating Cys and His residues in IFT172 proteins (***Figure 2F***).

These observations suggest that IFT172C3 is not a classical RING domain but rather resembles a U-box domain. U-box/RING domains mechanistically function by binding the ubiquitin-loaded E2 enzyme (E2-Ub conjugate), thus restricting the E2-Ub conjugate to conformations that facilitate ubiquitin transfer to the substrate (***Ozkan et al., 2005***; ***Dou et al., 2012b***; ***Plechanovová et al., 2012***; ***Soss et al., 2013***). Interestingly, structural comparisons with well-characterized U-box domains indicate that the predicted E2 binding site in HsIFT172C3 is structurally occluded by TPRs preceding the U-box domain (***Figure 2E***). Structural occlusion of the E2 binding site is a prominent mechanism of

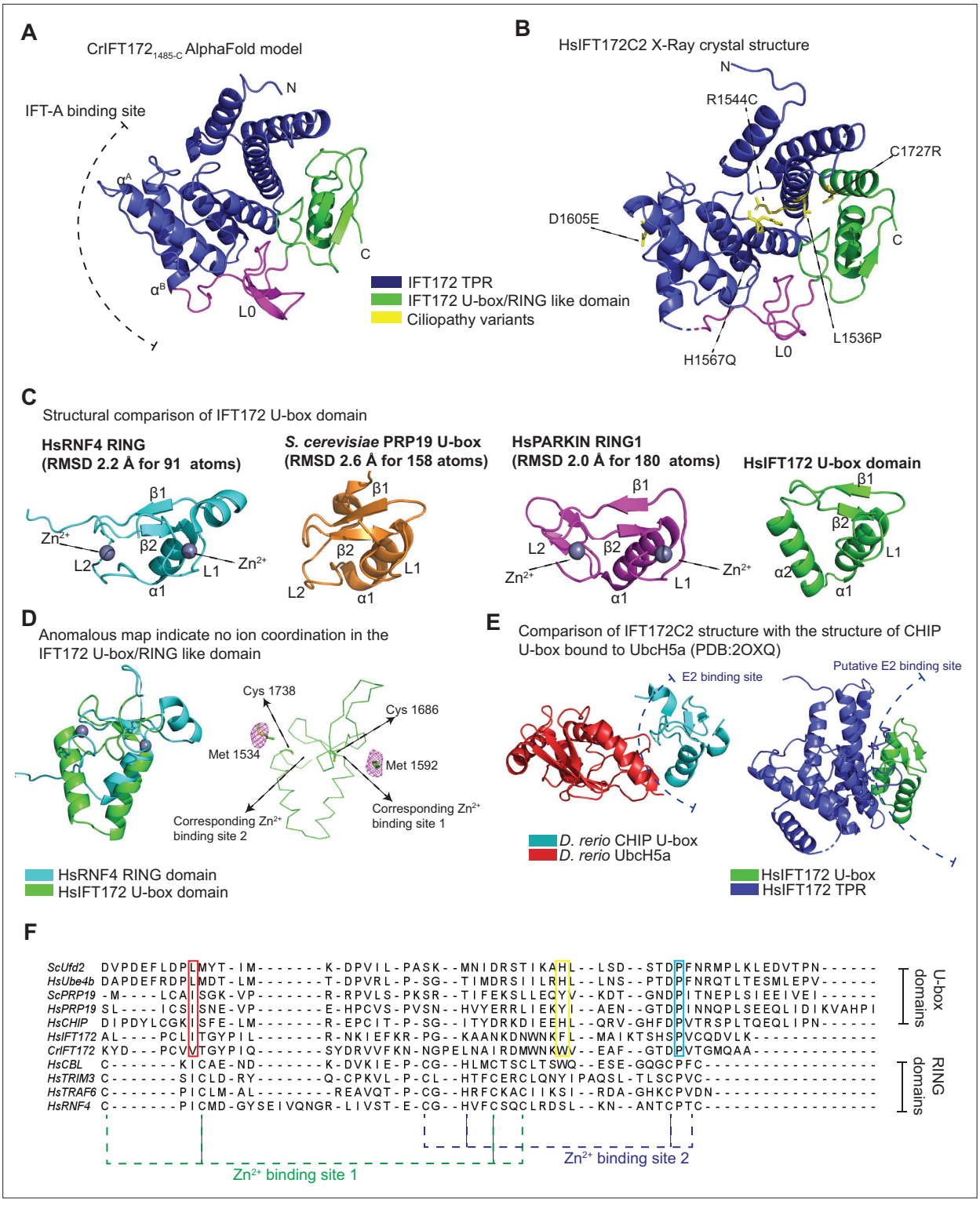


Figure 2. IFT172 contains a U-box-like domain distal to the IFT-A binding site. (**A**) Cartoon representation of the AlphaFold-predicted structure of the C-terminal residues 1485–1755 of CrIFT172. This globular domain comprises several TPR helices, including the IFT140/144 binding αA and αB helices, followed by a loop region (L0) and a U-box/RING-like motif. (**B**) Cartoon representation of the 2.1 Å resolution X-ray crystal structure of HsIFT172C2. The structure exhibits a similar fold to the CrIFT172$_{1485-1755}$ AlphaFold model, composed of TPR helices followed by a loop region (L0) and a U-box/RING-like motif. (**C**) Structural comparison of the U-box/RING-like motif in HsIFT172 with canonical RING domains of HsRNF4 (PDB: 4PPE), RING1 domain of PARKIN (PDB: 6HUE), and U-box domain of ScPRP19 (PDB: 6BAY), indicating the corresponding RMSD after superposition with the IFT172 motif. The U-box/RING-like motif in HsIFT172 superposes well with several structural components of U-box/RING domains, including the first loop (L1), the

Figure 2 continued on next page

Figure 2 continued

following beta strands (β1 and β2), and the helix (α1). A major difference in this HsIFT172 motif is the replacement of the characteristic second loop region (L2) found in U-box/RING domains with an alpha helix (α2). (**D**) (Left) Structural superposition of the IFT172 U-box/RING-like domain with the RING domain of RNF4, identifying corresponding Zn^{2+} binding sites. Zn^{2+} ions in RNF4 are depicted as grey spheres. (Right) Anomalous density map represented as a magenta mesh contoured at 5σ, obtained from HsIFT172C2 selenium-methionine substituted protein crystals. Anomalous density depicted in proximity to the U-box/RING-like domain. Cys residues and neighboring Met residues in the predicted Zn^{2+} binding site of IFT172 are represented as sticks. (**E**) (Left) Structure of the U-box domain in *Danio rerio* CHIP bound to *D. rerio* UbcH5a (PDB: 2OXQ), indicating the E2 binding site on the CHIP U-box domain. (Right) Comparison of HsIFT172C2 crystal structure with PDB: 2OXQ indicates the putative E2 binding site on IFT172 U-box is occluded by the IFT172 TPR domain. (**F**) Sequence alignment of U-box domains in HsIFT172 and CrIFT172 with several canonical U-box/RING domains. Zn^{2+} coordinating residues on RING domains are highlighted. Selected functionally relevant residues on U-box domains are depicted in boxes, and corresponding residues are also observed in the IFT172 U-box domain sequence.

The online version of this article includes the following source data and figure supplement(s) for figure 2:

Figure supplement 1. Purification and structure determination of HsIFT172 C-terminal domain.

Figure supplement 1—source data 1. Uncropped labelled Coomassie-stained SDS-PAGE gel of purified His-3C-tagged human IFT172 1470-C used to generate ***Figure 2—figure supplement 1A***.

Figure supplement 1—source data 2. Original unprocessed raw image file (TIFF) of the Coomassie-stained gel shown in ***Figure 2—figure supplement 1A***.

self-regulation seen in E3 ligases (***Buetow and Huang, 2016***; ***Dou et al., 2012a***; ***Trempe et al., 2013***; ***de Moura et al., 2018***). We conclude that IFT172 contains a U-box-like domain of unknown function at the C-terminus, which is a hotspot for ciliopathy patient variants.

IFT172 undergoes ubiquitination in the presence of the Ubch5a E2 enzyme

Given the structural similarity of HsIFT172C3 to U-box domains of well-characterized E3 ubiquitin ligases, we decided to test if IFT172 exhibits ubiquitination activity. To this end, various C-terminal constructs of Cr and Hs IFT172 proteins were tested in in vitro ubiquitination assays in the presence of purified MmUbe1 (E1 enzyme), ubiquitin, UbcH5a (E2 enzyme), and ATP (***Figure 3A***). Appearance of ubiquitin conjugates was observed in reactions containing $CrIFT172_{968\text{-}C}$ and $HsIFT172_{970\text{-}C}$ ($HsIFT172_{970\text{-}C}$ will be referred to as HsIFT172C1 from hereon). In the presence of ubiquitination pathway components (E1, E2, and ATP), ubiquitin ligases have the characteristic property of self-ubiquitination (auto-ubiquitination) in vitro (***Hatakeyama et al., 2001***; ***de Bie and Ciechanover, 2011***). Screening activity for HsIFT172C1 with 11 different E2 enzymes revealed the appearance of ubiquitin conjugates only in the presence of members of the Ubch5 E2 enzyme family (***Figure 3B***). The molecular mass of the ubiquitin conjugate is consistent with mono-ubiquitinated HsIFT172C1 used in the assay (***Figure 3A and B***) and is also stained by anti-His antibodies detecting the His-tag on HsIFT172C1 (***Figure 3C***). Polyubiquitination is a hallmark of E3 ubiquitin ligases resulting in an observed smear of ubiquitinated products on ub-antibody stained western blots (***Hatakeyama et al., 2001***). A characteristic smear is not observed in the case of IFT172 but rather a strong band corresponding to mono-ubiquitination is observed. Interestingly, higher molecular weight ubiquitinated bands of lower intensity that migrate close to the prominent mono-ubiquitinated IFT172 are observed in several replicates (***Figure 3A, B and F***). These bands could potentially correspond to additional mono-ubiquitination events on IFT172 or the formation of short poly-ubiquitin chains on IFT172.

Additional control experiments show that ubiquitin conjugates are only formed in the presence of all ubiquitination pathway components (E1, E2, ATP, and ubiquitin) but not observed when WT UbcH5a is replaced by a catalytically dead mutant (***Figure 3D***). Furthermore, the observed HsIFT172C1 ubiquitin conjugates disappear upon incubation with the Usp2 deubiquitinase enzyme and the HsIFT172C1 ubiquitin conjugate is resistant to reducing SDS-PAGE analysis (***Figure 3—figure supplement 1A and B***). Combined, these observations indicate a canonical lysine-linked ubiquitin conjugation occurring on HsIFT172C1 in the presence of UbcH5a.

We were unable to test the U-box domain alone as the untagged HsIFT172C3 construct did not yield soluble protein expression. We did obtain protein expression for a GST-tagged HsIFT172C3 construct but several proteolytically cleaved fragments co-purified suggesting that the U-box domain was partly degraded. Neither this GST-tagged HsIFT172C3 nor the HsIFT172C2 protein showed any ubiquitin conjugation (***Figure 3A***). However, the longer $CrIFT172_{968\text{-}C}$ and HsIFT172C1 did exhibit

Table 1. X-ray diffraction data collection and refinement statistics (PDB: 9H2D).

Two protein copies / asymmetric unit	$HsIFT172_{1470\text{-}C}$ Native	$HsIFT172_{1470\text{-}C}$ Selenium methionine
Data collection		
Wavelength (Å)	1.006	0.9785
Resolution range (Å)	45.25–2.07 (2.10–2.07)	47.02–2.78 (2.95–2.78)
Space group	P 1 2_1 1	P 1 2_1 1
Unit cell (Å, °)	a=46.97 b=90.51 c=67.42 α=90 β=97.42 γ=90	a=47.47 b=90.63 c=67.81 α=90 β=97.93 γ=90
Total reflections	225,982 (10379)	84,456 (12152)
Unique reflections	34,028 (1631)	26,158 (3916)
Multiplicity	6.6 (6.4)	3.2 (3.1)
Completeness (%)	99.5 (96.2)	93.0 (85.9)
Mean I/sigma	9.7 (1.3)	8.3 (0.7)
Rpim	0.037 (0.483)	0.077 (1.65)
CC1/2	0.999 (0.777)	0.998 (0.494)
Refinement		
Resolution range (Å)	45.25–2.10 (2.17–2.10)	
Reflections for refinement	32556 (3050)	
Reflections for Rfree	1564 (151)	
Protein residues	532	
Number of atoms	4423	
Protein	24213	
Ligands	31	
Water (solvent)	179	
R-work	0.189 (0.367)	
R-free	0.238 (0.370)	
Ramachandran favored (%)	97.35	
Ramachandran outliers (%)	0.00	
RMS bonds (Å)	0.01	
RMS angles (°)	1.23	
Average B-factors (Å ***Wan, 2018***)	65.14	

Statistics for the highest resolution shell are shown in parentheses.

ubiquitin conjugation (***Figure 3A***). Therefore, ubiquitination of HsIFT172 requires TPRs located N-terminally of the TPRs present in the crystallized construct shown in ***Figure 2B***, likely providing the ubiquitin accepting lysines.

We note that, unlike the canonical U-box/RING domain-containing proteins, IFT172 is not strongly polyubiquitinated in vitro. Moreover, Ubch5 proteins are highly reactive and often exhibit E3-independent ubiquitin transfer activity (***Hoeller et al., 2007***) and it is thus possible that the observed

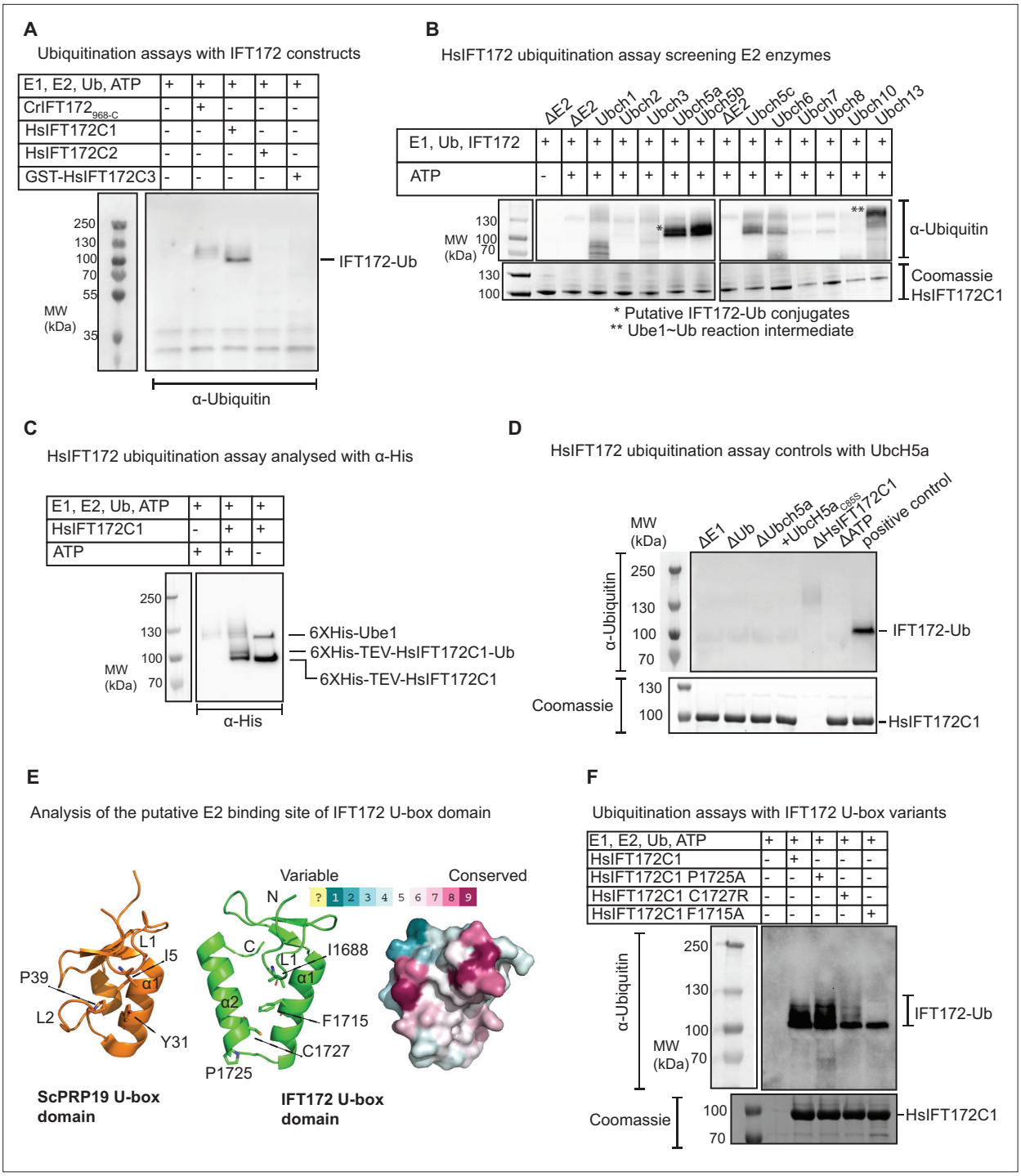


Figure 3. IFT172 exhibits ubiquitin conjugation activity in the presence of UbcH5a. (**A**) Western blot analysis of an in vitro ubiquitination assay containing *Mus musculus* Ube1 (E1), HsUbcH5a (E2), Ubiquitin (Ub), and ATP in the presence of various C-terminal IFT172 constructs as potential E3 ligases. Reactions were visualized by immunostaining with anti-Ubiquitin antibody. (**B**) Western blot analysis of in vitro ubiquitination assays containing Ube1 (E1), Ub, ATP, and HsIFT172C1, in the presence of 11 different ubiquitin-conjugating E2 enzymes (Abcam #ab139472). Reactions were visualized by immunostaining with (top) anti-Ubiquitin antibody and (bottom) Coomassie staining. Reactions were conducted under non-reducing conditions, accounting for the visualization of significant amounts of E1~Ub conjugate in the blot. (**C**) In vitro ubiquitination assays containing *M. musculus* 6XHis-Ube1, 6XHis-TEV-HsUbcH5a, Ub, and 6XHis-TEV-HsIFT172C1. Reactions were visualized by immunostaining with an anti-His tag antibody. (**D**) Western blot analysis of in vitro ubiquitination reactions containing *M. musculus* Ube1 (E1), HsUbcH5a (E2) WT/C85S mutant, Ubiquitin (Ub), HsIFT172C1, and ATP. As specified in each reaction, a reaction component was omitted (indicated by Δ) or a mutant component was used instead of the corresponding WT component (indicated by +). Reactions were visualized by immunostaining with (top) anti-Ubiquitin antibody and (bottom) Coomassie staining. (**E**)

Figure 3 continued on next page

Figure 3 continued

Analysis of the putative E2 binding site in the (center) HsIFT172 U-box domain and (left) U-box domain of ScPRP19. Both U-box domains are shown facing the E2 binding site. The PRP19 residues I5, Y31, and P39 whose mutagenesis leads to the loss of its ubiquitin ligase activity are represented as sticks (also highlighted in boxes within the sequence alignment in ***Figure 2E***). The equivalent residues in the putative E2 binding site of IFT172 are also depicted as sticks. (Right) Surface amino acid conservation map for the E2 binding site in IFT172 U-box domain, color-coded as indicated. (**F**) Western blot analysis of in vitro ubiquitination assay with HsIFT172C1 WT and the specified HsIFT172C1 U-box variants. Reactions were visualized by immunostaining with (top) anti-Ubiquitin antibody and (bottom) Coomassie staining.

The online version of this article includes the following source data and figure supplement(s) for figure 3:

Source data 1. Uncropped labelled blot and Coomassie images (anti-Ubiquitin and anti-His western blots plus Coomassie-stained gels) underlying the in vitro ubiquitination assays shown in ***Figure 3A–D and F***.

Source data 2. Original unprocessed raw image files of the blots, anti-Ubiquitin and anti-His western blots, and Coomassie-stained gels underlying ***Figure 3A–D and F***.

Figure supplement 1. Purification and ubiquitination assays with HsIFT172C constructs.

Figure supplement 1—source data 1. Uncropped labelled blot and Coomassie images (anti-Ubiquitin and anti-His western blots plus Coomassie-stained gels) underlying ***Figure 3—figure supplement 1A–F***.

Figure supplement 1—source data 2. Original unprocessed raw image files of the blots, anti-Ubiquitin and anti-His western blots, and Coomassie-stained gels underlying ***Figure 3—figure supplement 1A–F***.

IFT172 ubiquitination is a result of U-box-independent Ubch5 activity. As deletion of the U-box domain rendered IFT172 constructs insoluble in *Escherichia coli*, we pursued mutagenesis studies on the U-box domain in the context of the HsIFT172C1 construct. A common method to inactivate U-box/RING domains is to disrupt E2 binding (***Garcia-Barcena et al., 2020***). Comparisons of the IFT172 sequence (***Figure 2F***) and structure (***Figure 3E***) with well-characterized U-box domains indicated two potential E2 binding residues in the IFT172 U-box domain. This includes a highly conserved Ile/Leu residue (I1688 in HsIFT172) in loop L1 of U-box/RING domains (***Ohi et al., 2003***; ***Garcia-Barcena et al., 2020***; ***Figure 3E***) and highlighted with a red box in ***Figure 2F*** involved in E2 binding. Secondly, a conserved aromatic residue (F1715 in HsIFT172) is commonly found in helix α1 of U-box/RING domains (***Ohi et al., 2003***; ***Zheng et al., 2000***; ***Figure 3E***) and highlighted with a yellow box in ***Figure 2F*** where it contributes to E2 binding. Finally, a completely conserved proline residue is found in the loop L2 of U-box domains (***Ohi et al., 2003***; ***Hatakeyama et al., 2001***; P1725 in HsIFT172, see ***Figures 2F and 3E***), which in IFT172 caps the N-terminus of alpha-helix α2. Mutation of this conserved proline residue results in a complete loss of ubiquitination activity for four different U-box domain-containing proteins (***Hatakeyama et al., 2001***). Interestingly, the IFT172 ciliopathy variant C1727R (***Halbritter et al., 2013***) also maps to helix α2 in the U-box domain (***Figure 3E***). Notably, I1688 and F1715 are located near an evolutionarily conserved surface patch on the putative E2 binding site of IFT172 (***Figure 3E***). To test the importance of these residues in IFT172 ubiquitination, the residues Ile1688, Phe1715, and Pro1725 in IFT172 were mutated to alanine, whereas Cys1727 was mutated to arginine to mimic the patient variant. Soluble protein expression was obtained for each of the F1715A, P1725A, and C1727R HsIFT172C1 variants (but not for the I1688A variant) and the soluble proteins were purified (***Figure 3—figure supplement 1C–F***). In vitro ubiquitination assays show that while mono-ubiquitination is not affected in IFT172 mutants, significant loss of the higher molecular weight bands for ubiquitinated IFT172 was observed for the F1715A and C1727R variants (***Figure 3F***). IFT172 ubiquitin conjugation is thus affected by mutations of the putative E2 binding site of IFT172 U-box domain. We note that the strong mono-ubiquitination of IFT172 observed in ***Figure 3F*** is likely U-box-independent ubiquitination by the E2 enzyme as this activity is not affected by IFT172 U-box mutations. In summary, we conclude that IFT172 exhibits ubiquitin conjugation in the presence of UbcH5a that is reduced in E2-binding and ciliopathy variants of IFT172. Therefore, while mutations in the IFT172 U-box domain affect the formation of higher molecular weight ubiquitin conjugates, the prominent mono-ubiquitination of IFT172 is likely attributable to the E3-independent activity of UbcH5a, as this event is not impacted by these U-box mutations, rather than indicating an intrinsic auto-ubiquitination capacity of IFT172 itself.

IFT172 U-box domain pulls down ubiquitin in vitro

To further assess the biochemical properties of IFT172, we carried out interaction studies of HsIFT172C2 with stable mimics of the E2~Ub (UbcH5a~Ub) conjugate. To this end, the UbcH5a active

site cysteine was mutated to a serine, which allowed for the production and purification of a stable oxyester-linked UbcH5a~Ub conjugate (***Middleton et al., 2014***), which mimics the native thioester-linked E2-Ub conjugate. Interactions between IFT172 and the UbcH5a~Ub conjugates were analyzed by affinity pull-downs using GST-tagged HsIFT172C2 (***Figure 4A***, ***Figure 4—figure supplement 1C***) showing an interaction between IFT172C2 and the WT UbcH5a~Ub conjugate. Additionally, we produced and tested two point-mutants of the UbcH5a~Ub conjugate (UbcH5a F62A or A96D) known to disrupt interaction with U-box/RING domains (***Gundogdu and Walden, 2019***; ***Levin et al., 2010***; ***Xu et al., 2008***). However, these mutations did not prevent the interaction between UbcH5a~Ub and HsIFT172C2 (***Figure 4A***). Moreover, structural modeling of a hetero-dimeric complex between HsIFT172C3 and UbcH5a using AF-M did not indicate a direct interaction (***Figure 4B***). In silico screening of complex formation between IFT172C3 and each of the 40 annotated Hs E2 enzymes also did not reveal confident complex formation with any of the E2 enzymes (data not shown). Combined, this indicates that although IFT172 associates with the E2-Ub conjugate in pull-downs, this association may not be mediated by direct interactions with the E2 enzyme (***Figure 4A***).

Alternatively, the interaction between IFT172 and UbcH5a~Ub could be mediated through ubiquitin. Indeed, several crystal structures have elucidated the RING-E2~Ub interaction, demonstrating direct interactions between the RING domain and ubiquitin (***Dou et al., 2012b***; ***Plechanovová et al., 2012***; ***Buetow and Huang, 2016***). Given that E2 mutations do not abolish the interaction between UbcH5a~Ub and HsIFT172C2, we reasoned that the interaction could be mediated by ubiquitin. N-terminally linked tetra-ubiquitin chains were pulled down with GST-tagged HsIFT172C2 indicating an IFT172-ubiquitin interaction (***Figure 4C***). To test if the conserved IFT144 and IFT140 binding site on IFT172 is involved in ubiquitin binding, a pull-down was carried out with tetra-ubiquitin with the HsIFT172C2_D1605R mutant. Asp1605 corresponds to a previously reported human ciliopathy locus (***Bujakowska et al., 2015***) that maps onto the corresponding IFT144 and IFT140 binding site on IFT172. This HsIFT172C2_D1605R mutation does not appear to influence the binding to ubiquitin (***Figure 4C***). Pull-down of the tetra-ubiquitin chain with GST-tagged HsIFT172C2 or HsIFT172C3 showed that both constructs retain tetra-ubiquitin-binding activity (***Figure 4D***). The signal observed for HsIFT172C3 was somewhat reduced compared to HsIFT172C2, which likely reflects the partial proteolytic degradation of the GST-HsIFT172C3 construct during purification (***Figure 4—figure supplement 1B***) rather than an intrinsic difference in ubiquitin-binding affinity. This suggests that the U-box domain likely contains the ubiquitin-binding site. Indeed, AF-M modeling of the IFT172 U-box domain with ubiquitin suggests the formation of a complex between the IFT172 U-box and ubiquitin (***Figure 4E and F***). It was previously reported that E2 enzymes catalyze the E3-independent mono-ubiquitination of proteins containing a UBD (***Hoeller et al., 2007***). It is thus possible that the mono-ubiquitination of HsIFT172C1 observed in the presence of UbcH5a (***Figure 3***) could be a result of the ubiquitin-binding capability of HsIFT172C1.

Loss of IFT172 U-box domain impairs protein stability and leads to ciliogenesis defects in RPE1 cells

To investigate the cilium-specific functions of the U-box domain of IFT172, we used CRISPR/Cas12a to engineer human RPE1 cell lines carrying a deletion of the IFT172 U-box domain. These cell lines were used to assess the impact of U-box domain loss on ciliogenesis, ciliary IFT172 localization, and TGFβ-1- and PDGF-DD-stimulated signaling responses (***Figure 5***, ***Figure 5—figure supplement 1***). A schematic overview and nomenclature for the four generated GFP-tagged RPE1 cell lines are shown in ***Figure 5A***, with a detailed description of the cell line generation strategy provided in the Materials and methods section (***Figure 5—figure supplement 2A and B***, ***Figure 5—figure supplement 3A and B***). To validate the engineered lines, we performed Sanger sequencing to confirm precise GFP knock-in and to verify the absence of undesired insertions or deletions (indels; ***Figure 5—figure supplement 2C***, ***Figure 5—figure supplement 3C***). Expression of the tagged full-length and U-box-truncated IFT172 proteins was confirmed by immunoblotting with an anti-IFT172 antibody, which additionally revealed reduced steady-state levels of the IFT172ΔU-box protein compared to full-length IFT172, indicating that loss of the U-box domain compromises IFT172 protein stability (***Figure 5—figure supplement 4***). Ciliogenesis in these cells was induced by serum withdrawal for 24 hr and cilia were visualized by staining for acetylated tubulin. In cells with a homozygous IFT172 U-box domain deletion, cilia formation was severely reduced compared to cells expressing GFP-tagged full-length IFT172 (***Figure 5B***).

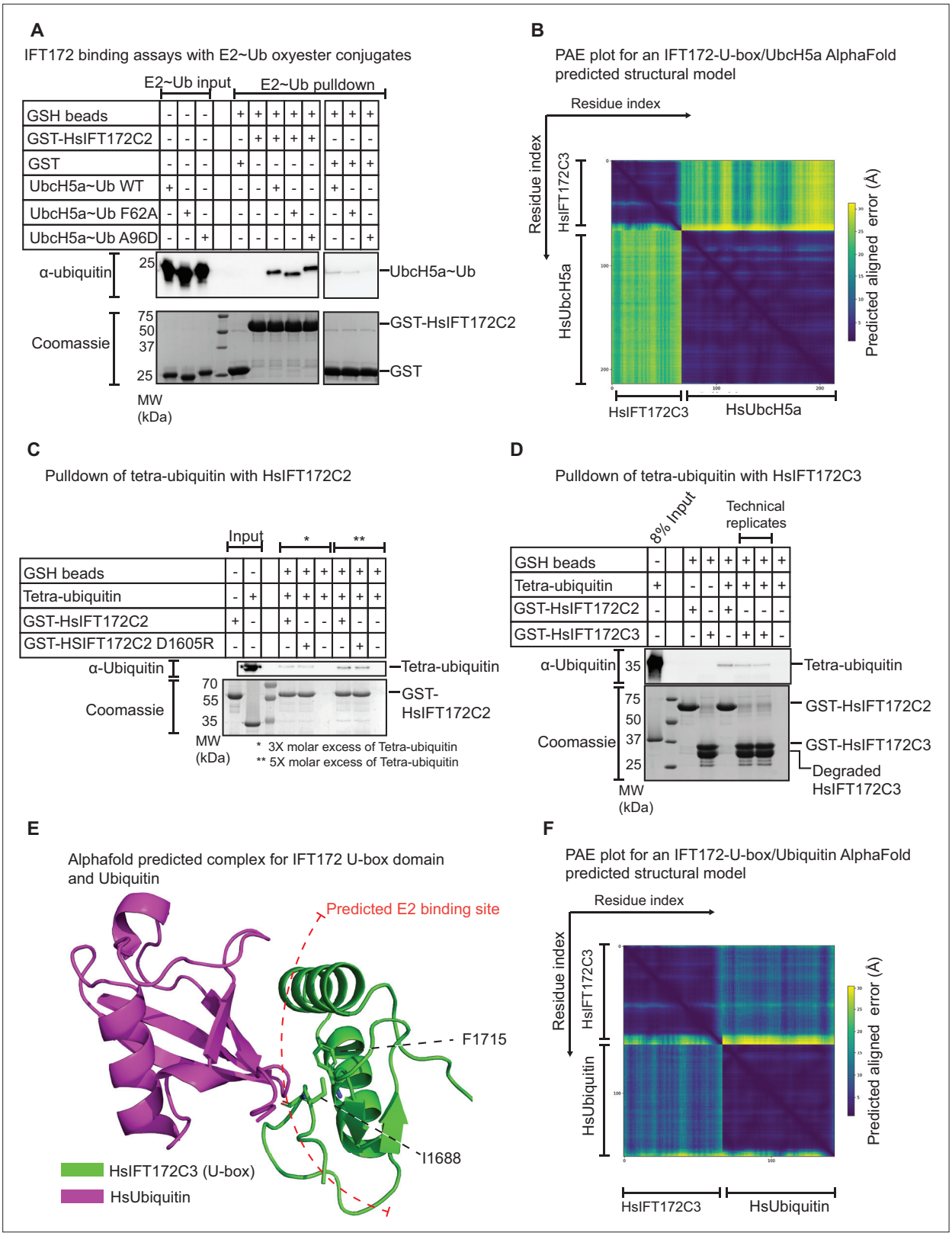


Figure 4. IFT172 U-box domain is a binding site for ubiquitin. (**A**) Pull-down of purified UbcH5a$_{C85S}$~Ub conjugates with GST-tagged HsIFT172C2 immobilized on GSH beads. Samples after elution were analyzed by western blotting with (top) anti-ubiquitin antibody and (bottom) Coomassie staining. Input shown is 2% for the western blot and 7.8% for the Coomassie staining. (**B**) PAE plot for an AlphaFold-generated structural model for a complex between HsIFT172C3 and HsUbcH5a. High error values are observed for interchain residue pairs, suggesting no high confidence prediction

Figure 4 continued on next page

Figure 4 continued

for an interaction between the two chains. (**C**) Pull-down of tetra-ubiquitin with GST-tagged HsIFT172C2 constructs immobilized on GSH beads. The D1605R mutation on the IFT-A binding site of HsIFT172C2 does not impact the binding of tetra-ubiquitin to HsIFT172C2. Reactions were visualized by immunostaining with (top) anti-ubiquitin antibody and (bottom) Coomassie staining. (**D**) Pull-down of tetra-ubiquitin with various GST-tagged HsIFT172 constructs immobilized on GSH beads. Both HsIFT172C2 and HsIFT172C3 pull-down tetra-ubiquitin at similar levels. The prominent lower molecular weight band in the HsIFT172C3 sample is a degradation/proteolytic cleavage product obtained upon HsIFT172C3 expression and purification from *E. coli*. The two lanes showing a pull-down of tetra-ubiquitin with HsIFT172C3 represent technical replicates. Reactions were visualized by immunostaining with (top) anti-Ubiquitin antibody and (bottom) Coomassie staining. (**E**) AlphaFold-predicted structural model for a complex between HsIFT172C3 and HsUbiquitin. The model suggests that ubiquitin binds to the predicted E2~Ub binding site of HsIFT172C3. The predicted E2 binding residues of the HsIFT172 U-box domain are depicted in the model. (**F**) PAE plot for the AlphaFold structural model shown in panel E. Moderate PAE scores are observed for the residue pairs corresponding to the interaction interface (panel E) between the two chains.

The online version of this article includes the following source data and figure supplement(s) for figure 4:

Source data 1. Uncropped labelled α-Ubiquitin blot images and corresponding Coomassie-stained gels of the GST-HsIFT172C2/C3 ubiquitin pulldown assays underlying ***Figure 4A, C and D***.

Source data 2. Original unprocessed raw α-Ubiquitin blot and Coomassie-stained gel image files of the GST-HsIFT172C2/C3 ubiquitin pulldown assays underlying ***Figure 4A, C and D***.

Figure supplement 1. Purification of GST-tagged HsIFT172 constructs and of the E2~Ub conjugate.

Figure supplement 1—source data 1. Uncropped labelled Coomassie-stained gels showing purified His-GST-HsIFT172C2, His-GST-HsIFT172C3 and the UbcH5a(C85S)~Ub conjugate underlying ***Figure 4—figure supplement 1***.

Figure supplement 1—source data 2. Original unprocessed raw Coomassie-stained gel image files showing purified His-GST-HsIFT172C2, His-GST-HsIFT172C3 and the UbcH5a(C85S)~Ub conjugate underlying ***Figure 4—figure supplement 1***.

Moreover, cilia that are retained in the IFT172ΔU-box (homozygous) cells are significantly shorter, with a median cilia length of ~1.3 μm in IFT172ΔU-box (homozygous) cells, compared to ~3.0 μm in IFT172-FL (homozygous) cells (***Figure 5B***). Meanwhile, in cells with a heterozygous IFT172 U-box domain deletion, no significant effect on ciliation or ciliary length was observed (***Figure 5B***). To further investigate the observed ciliogenesis phenotype, the localization of the eGFP-tagged IFT172 proteins was analyzed by immunofluorescence microscopy, along with quantification of fluorescence signal along the ciliary axis. Both the full-length IFT172 protein as well as the IFT172ΔU-box truncation were recruited to the cilium (***Figure 5C***, ***Figure 5—figure supplement 1C***). The full-length IFT172 protein is present along the length of the axoneme, with notable accumulations at the ciliary base and tip. In the cells with a homozygous IFT172 U-box deletion, eGFP-tagged IFT172ΔU-box protein is accumulated along the short axoneme (***Figure 5—figure supplement 1E***), but in heterozygous cells that form normal length cilia, the distribution of the eGFP-tagged IFT172ΔU-box protein is similar to the full-length IFT172 protein (***Figure 5C***, ***Figure 5—figure supplement 1D and F***). This consistent localization pattern suggests that the U-box domain is not essential for IFT172 trafficking to or within the cilium, despite its impact on overall protein levels and ciliogenesis.

Examination of protein expression levels using immunostaining revealed a striking reduction in the levels of the U-box deleted IFT172 protein (***Figure 5D***). The specific IFT172 antibody used here was generated against an HsIFT172 epitope (amino acids 1353–1652) that lies outside the U-box domain. The reduced detection of IFT172 is thus most likely due to reduced protein expression or stability levels upon U-box deletion. As IFT172 is known to be essential for ciliogenesis (***Tsao and Gorovsky, 2008***; ***Pruski et al., 2019***), the severe reduction in expression levels of both IFT172 alleles causes ciliogenesis defects in the IFT172ΔU-box (homozygous) cells. Meanwhile, in the IFT172ΔU-box (heterozygous) cells, the observed upregulation in the WT IFT172 allele compensates for the reduced expression levels of the U-box truncated IFT172 allele (***Figure 5D***), which likely provides sufficient IFT172 for ciliogenesis at a similar level as the parental RPE1 cells (***Figure 5B***). However, the IFT172ΔU-box protein contains both IFT-A and IFT-B binding sites required for incorporation into IFT trains, and the IFT172ΔU-box (heterozygous) cells will thus have a reduction in the concentration of IFT172 with a U-box domain as compared to parental cells.

IFT172 U-box domain influences TGF-β signaling

Given that the U-box deleted IFT172 still localizes to the cilium (***Figure 5C***), we wanted to investigate if ciliary signaling events are impacted by the loss of the IFT172 U-box domain. The severe ciliogenesis defects exhibited by the IFT172ΔU-box (homozygous) cells (***Figure 5B***) will result in

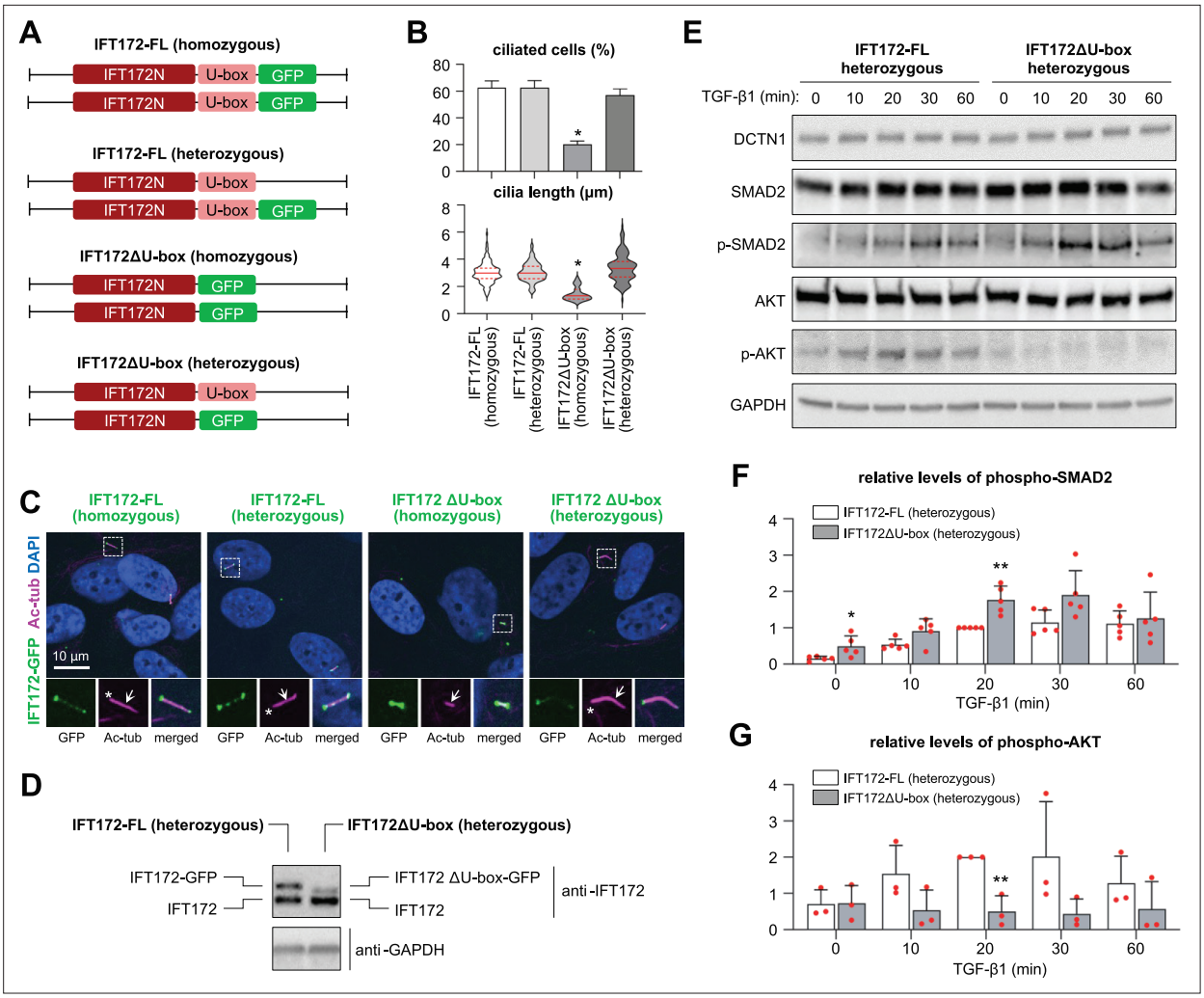


Figure 5. Truncation of the IFT172 U-box domain impairs ciliogenesis and leads to altered TGF-β signaling response in RPE1 cells. (**A**) Schematic representation and nomenclature of RPE1 cell lines generated by CRISPR/Cas12a-mediated exon targeting of the IFT172 gene. (**B**) Quantification of ciliogenesis (percentage of ciliated cells, upper panel) and ciliary length (lower panel) in all RPE1 cell lines. Error bars in the upper panel represent SEM (*: p<0.05). (**C**) IFM analysis of IFT172-GFP (*green*) localization to primary cilia (acetylated tubulin Ac-tub., *purple*) in RPE1 cell lines. Nuclei are stained with DAPI (*blue*). The top row displays whole-cell views, while the bottom row panels show zoomed-in insets of the cilium (arrows). Asterisks indicate ciliary base region. (**D**) WB analysis of IFT172 expression in IFT172-FL (heterozygous) and IFT172ΔU-box (heterozygous) RPE1 cell lines. (**E**) WB analysis of phosphorylation levels of SMAD2 (p-SMAD2) and AKT (p-AKT; p-AKT^{T308}) in IFT172-FL (heterozygous) and IFT172ΔU-box (heterozygous) RPE1 cell lines treated with 2 ng/mL TGF-β1 ligand for the indicated time points. (**F, G**) Quantification of p-SMAD2 (**F**) and p-AKT (**G**) levels from panel E, normalized to DCTN1 and GAPDH. Error bars represent SEM (*: p<0.05; **: p<0.01).

The online version of this article includes the following source data and figure supplement(s) for figure 5:

Source data 1. Uncropped labelled western blot acquisitions (α-IFT172, α-GAPDH, DCTN1, SMAD2, p-SMAD2, AKT, p-AKT) from IFT172-FL and IFT172ΔU-box cell lines across a TGF-β1 stimulation time course underlying ***Figure 5D and E***.

Source data 2. Original unprocessed raw western blot image files (IFT172, GAPDH, DCTN1, SMAD2, p-SMAD2, AKT, p-AKT) from the IFT172-FL and IFT172ΔU-box TGF-β1 stimulation time course underlying ***Figure 5D and E***.

Figure supplement 1. Truncation of the IFT172 U-box domain does not impair PDGF-DD-mediated AKT signaling and ciliary IFT172 localization in RPE1 cells.

Figure supplement 1—source data 1. Uncropped labelled western blot acquisitions (DCTN1, AKT, p-AKT T308, p-AKT S473, GAPDH) from IFT172-FL and IFT172ΔU-box cell lines across a PDGF-DD stimulation time course underlying ***Figure 5—figure supplement 1A***.

Figure supplement 1—source data 2. Original, uncropped raw images for the western blot analysis shown in ***Figure 5—figure supplement 1A*** (DCTN1, total AKT, phospho-AKT Thr308, phospho-AKT Ser473 and GAPDH loading control).

Figure supplement 2. Sequence analysis of GFP-tagged full-length IFT172 clones.

Figure 5 continued on next page

Figure 5 continued

Figure supplement 2—source data 1. Original, uncropped genotyping PCR gel for ***Figure 5—figure supplement 2***, with the wild-type and eGFP-tagged IFT172 alleles indicated.

Figure supplement 2—source data 2. Original raw image of the genotyping PCR agarose gel from ***Figure 5—figure supplement 2***, showing the wild-type and eGFP-tagged IFT172 alleles.

Figure supplement 3. Sequence analysis of GFP-tagged U-box-truncated IFT172 clones.

Figure supplement 3—source data 1. Uncropped labelled agarose gel images of the genotyping PCRs identifying the wildtype and tagged IFT172 alleles underlying ***Figure 5—figure supplement 3***.

Figure supplement 3—source data 2. Original unprocessed raw agarose gel image files of the genotyping PCRs identifying the wildtype and tagged IFT172 alleles underlying ***Figure 5—figure supplement 3***.

Figure supplement 4. Immunoblot analysis of IFT172 expression in the engineered RPE1 cell lines.

Figure supplement 4—source data 1. Uncropped labelled western blot images probed for IFT172 and α-tubulin underlying ***Figure 5—figure supplement 4***.

Figure supplement 4—source data 2. Original unprocessed raw western blot image files probed for IFT172 and α-tubulin underlying ***Figure 5—figure supplement 4***.

U-box-independent secondary effects that may affect signaling responses. Therefore, we focused our attention on the IFT172ΔU-box (heterozygous) cells that possess normal ciliation and initially investigated TGF-β signaling in these mutant cells. To this end, previous studies showed that the primary cilium regulates both canonical and non-canonical branches of TGF-β signaling (***Clement et al., 2013***; ***Doganli, 2024***), the former operating through activation of R-SMAD transcription factors at the ciliary pocket, where ciliary receptors are internalized for phosphorylation of SMAD2/3 (***Clement et al., 2013***). Compared to control cells, IFT172ΔU-box (heterozygous) cells showed an increased level of SMAD2 activation upon TGF-β1 stimulation, and the level of SMAD2 phosphorylation also appeared slightly elevated in unstimulated heterozygous IFT172ΔU-box cells (***Figure 5E and F***). In contrast, TGF-β1-mediated activation of AKT, which operates in the non-canonical branch of TGF-β signaling, was markedly reduced in heterozygous IFT172ΔU-box cells (***Figure 5E and G***). We further evaluated AKT activation in response to PDGF-DD stimulation, which activates the homodimer of PDGFRB outside and independent of the primary cilium (***Nielsen et al., 2015***). In this case, PDGF-DD-induced activation of AKT was unaffected in the heterozygous IFT172ΔU-box cells (***Figure 5—figure supplement 1A and B***). Thus, perturbation to the IFT172 U-box domain results in differential effects on TGF-β-mediated signaling pathways, for which the U-box domain may play a regulatory role in the mechanisms by which the cilium balances the output of canonical versus non-canonical TGF-β pathways.

Discussion

IFT172 bridges IFT-A and IFT-B complexes in IFT trains

This study provides new insights into the structure and function of IFT172, a key component of the IFT machinery. The N-terminal region of IFT172 is known to form inter-IFT subunit interactions with the IFT-B subunits IFT57/IFT80 (***Taschner et al., 2016***; ***Petriman et al., 2022***; ***Wang et al., 2018***), while much less was known about the C-terminal part of IFT172. Our comprehensive structural and biochemical analyses reveal two functionally relevant motifs at the C-terminus of IFT172: a TPR motif involved in IFT-A association and a U-box-like domain likely involved in ciliary ubiquitination events. These discoveries not only enhance our understanding of the role of IFT172 in IFT but also suggest new mechanisms for the regulation of ciliary function.

Early studies on IFT172 hypothesized a function in anterograde to retrograde transition of IFT trains at the ciliary tip (***Pedersen et al., 2005***). This hypothesis was based on the observation that the *C. reinhardtii fla11* strain with a C-terminal missense mutation in IFT172 leads to an accumulation of IFT proteins at the ciliary tip, a phenotype characteristic of retrograde IFT defects (***Pedersen et al., 2005***). Our findings now provide a molecular basis for the retrograde IFT phenotype observed in the *fla11* strain. We show that the FLA11 mutation lies in the TPR motif of IFT172 directly associating with IFT subunits IFT144 and IFT140 (***Figure 1***, ***Figure 1—figure supplement 1***). This suggests that impairment of the association of IFT172 with IFT-A likely underlies the faulty switch to retrograde IFT.

Our results align with recent cryo-ET structures of anterograde and retrograde IFT trains, which show that the IFT172 C-terminus interacts with IFT144 in anterograde trains and with IFT140 in retrograde trains (***Lacey et al., 2023***; ***Lacey et al., 2024***). While L1615P is predicted to affect both interactions, the predominantly retrograde IFT phenotype of fla11 can be rationalized by the distinct roles of the IFT172 C-terminus in anterograde versus retrograde trains. In anterograde trains, the IFT172 C-terminus functions as a flexible tether in stoichiometric excess, where additional lateral interactions between IFT-B subunits provide redundancy that likely compensates for reduced affinity caused by L1615P46. In contrast, the retrograde train requires the IFT172 C-terminus to adopt a rigid conformation integral to the IFT-A dimeric interface, with no compensatory lateral interactions (***Lacey et al., 2024***). The helix-breaking L1615P mutation would thus selectively disrupt retrograde train assembly.

Interestingly, the human ciliopathy variant D1605E (***Bujakowska et al., 2015***) also localizes to the corresponding IFT-A interaction site in the *Hs*IFT172, suggesting that impaired IFT-A association contributes to disease manifestation. The additional methylene group in the glutamate side chain may introduce steric clashes at the tightly packed IFT172-IFT-A interface, providing a rationale for the pathogenicity of this conservative substitution. Collectively, these findings establish IFT172 as a key IFT subunit that bridges IFT-B and IFT-A complexes in both anterograde and retrograde IFT trains, providing a molecular basis for its involvement in ciliopathies.

We note that IFT-A subunits IFT121, IFT122, and IFT144 share a similar domain organization with IFT172, with TPR repeats terminating in small C-terminal Zn-finger-like domains (***Walia et al., 2019***). Structural superposition reveals a shared topology, raising the possibility that these domains share a common evolutionary origin. While this could suggest conserved ubiquitin-related functions across these subunits, the more parsimonious explanation is that these C-terminal domains primarily serve structural roles in protein stabilization or IFT subunit interactions. Indeed, we cannot exclude that the U-box-like domain of IFT172 similarly contributes to protein stability, as evidenced by the reduced IFT172 levels upon U-box deletion (***Figure 5D***). Whether the U-box-like domain of IFT172 has acquired an additional ubiquitin-related function beyond its structural role remains an open question requiring further investigation.

Stoichiometry and potential ubiquitin-related functions of IFT172 in IFT trains

Recent cryo-EM reconstructions of IFT trains have revealed a stoichiometry of 2:1 for IFT-B to IFT-A complexes (***Lacey et al., 2023***; ***Lacey et al., 2024***). This stoichiometry implies that only half of the IFT172 C-termini are engaged with IFT-A, while the remainder are potentially free to interact with other ciliary components. Our discovery of a U-box-like domain in IFT172 (***Figure 2***), and the identification of a UBX domain protein as an interaction partner, suggests potential ubiquitin-related functions for IFT172 within the cilium. These functions could extend beyond proteasomal degradation to include roles in ubiquitin-mediated protein trafficking or regulation. This hypothesis is supported by our observation of weak in vitro ubiquitin-conjugation of IFT172 (***Figure 3F***). Further demonstration of ubiquitination activity of IFT172 directly in cells by identifying *bona fide* ubiquitination substrates is required to assign the ubiquitin ligase function to IFT172.

The IFT172 U-box domain appears to be in an auto-inhibited state in our crystal structure of HsIFT172C2 (***Figure 2E***), potentially explaining the absence of a robust auto-ubiquitination activity in vitro. This structural inhibition is reminiscent of the RING ubiquitin ligase CBL (***Dou et al., 2012a***), where phosphorylation and substrate binding trigger a conformational change that activates ligase activity (***Dou et al., 2012a***; ***Kassenbrock and Anderson, 2004***). Intriguingly, the phosphosite database (***Hornbeck et al., 2015***) lists four residues (T1533, S1549, T1689, and Y1691) at the U-box/TPR interface as phosphorylation sites (***Figure 2—figure supplement 1D***). Phosphorylation of these residues could potentially alleviate the auto-inhibited state, suggesting a possible regulatory mechanism. Furthermore, a 30-residue linker connects the U-box domain to the last TPR of IFT172, likely providing significant conformational flexibility (***Figure 2A and B***). This flexibility may be functionally crucial for the U-box domain, allowing it to adopt different conformations as needed for its various roles. However, we note that the proposed autoinhibition model and its potential regulation by phosphorylation remain hypothetical and require future experimental validation.

Our biochemical characterization has further revealed ubiquitin-binding properties of IFT172, mapped to the U-box-like domain (***Figure 4***). While this property is atypical for U-box domains, it

bears resemblance to structurally related zinc finger domains, such as the UBZ domain with a β-β-α motif (**Bomar et al., 2007**). These domains function as UBDs regulating various cellular processes (**Bomar et al., 2007**). This finding is particularly intriguing as RING domains, which are structurally similar to U-box domains, are known to mediate contacts with ubiquitin for priming the E2-Ub conjugate for ubiquitin transfer (**Dou et al., 2012b**; **Plechanovová et al., 2012**).

The ubiquitin-binding capability of IFT172 could facilitate the trafficking or turnover of ubiquitinated proteins in the cilium, complementing known ubiquitin-dependent processes. For instance, signal-dependent ciliary exit of ubiquitinated GPCRs and the Hedgehog pathway component Smoothened (**Lv et al., 2021**; **Desai et al., 2020**) is mediated by UBDs in the adaptor protein TOM1L2 (**Shinde et al., 2020**; **Huang et al., 2009**). However, UBDs associated with several other cilium-associated signaling pathways and processes are yet to be identified. While IFT139 has been implicated in the ciliary turnover of ubiquitinated tubulin during ciliary disassembly (**Wang et al., 2019**), unlike TOM1L2, ubiquitin-binding sites have not been validated in IFT139 or any other BBSome or IFT subunits. This positions the IFT172 U-box domain as a potential UBD for the trafficking or turnover of ubiquitinated proteins in the cilium.

Implications of the IFT172 U-box domain in ciliary signaling

Several ciliopathy variants map to the C-terminal part of IFT172 and are located in the vicinity of the U-box domain (**Figure 2B**). These mutations could disrupt ubiquitin-related functions of the U-box domain or impair protein stability. To investigate the physiological relevance of the IFT172 U-box domain, we analyzed engineered RPE1 cells with U-box deletions. While homozygous deletion of the U-box domain significantly impaired total IFT172 protein levels and affected ciliogenesis, a heterozygous deletion maintained near-wild-type levels of total IFT172 protein and cilium formation (**Figure 5B–D**). In the heterozygous U-box-deleted cells, we observed altered SMAD2 phosphorylation levels (**Figure 5E and F**) and impaired AKT activation (**Figure 5E and G**) in response to TGF-β1 stimulation. These findings suggest that the U-box domain is crucial for protein stability and its deletion differentially affects the SMAD and non-SMAD TGF-β activation pathways. The final phenotypic outcome of TGF-β signaling depends on the balance and fine-tuning of both SMAD and non-SMAD activation pathways, as these pathways engage in extensive cross-talk and can mutually regulate each other (**Guo and Wang, 2009**; **Heldin and Moustakas, 2016**; **Zhang, 2009**). Our results suggest that IFT172, through its U-box domain, may play a crucial role in maintaining this balance. However, we note that our current experiments cannot distinguish whether these signaling effects result specifically from loss of ubiquitin-related functions of the U-box domain or from the reduced levels of functional IFT172 protein in the heterozygous U-box-deleted cells. Targeted point mutations that selectively disrupt ubiquitin binding without affecting protein stability would be required to resolve this question. We further note that our conclusions are based on a single validated clone per genotype, and confirmation in independent clones will be important to fully exclude clonal effects.

While ciliary regulation of SMAD2/3 phosphorylation via TGFβ receptors is well established, the connection between primary cilia and AKT signaling is also increasingly supported. AKT has been shown to regulate ciliogenesis initiation through a Rab11-effector switch mechanism, where disruption of AKT signaling promotes the transition from Rab11-WDR44 to the ciliogenic Rab11-FIP3-Rabin8 complex (**Shim et al., 2021**). Furthermore, a cilia-dependent reciprocal activation between AKT1 and SMAD2/3 has been demonstrated in trabecular meshwork cells, where primary cilia act as mechanosensors regulating both pathways (**Shim et al., 2021**). Our observation that heterozygous deletion of the IFT172 U-box domain differentially affects SMAD2 phosphorylation and AKT activation is consistent with the emerging role of primary cilia in coordinating canonical and non-canonical TGFβ signaling, although the precise mechanism by which the U-box domain influences these pathways requires further investigation.

In conclusion, our findings reveal that IFT172, beyond its structural role in IFT trains, has an unexpected function in signal regulation. The flexible nature of half of the IFT172 C-termini in IFT trains, combined with its ubiquitin-related activities, positions IFT172 as a potential regulator of ubiquitin-mediated processes within the cilium. This dual functionality - providing both structural support and signaling regulation - may explain why IFT172 mutations lead to such diverse ciliopathy phenotypes. These results expand our understanding of how IFT proteins contribute to ciliary signaling beyond their established roles in protein transport.

Materials and methods

Cloning and expression of proteins in *E. coli*

DNA sequences encoding the respective truncations of HsIFT172 and CrIFT172, as well as full-length HsUbiquitin and HsUbcH5a, were polymerase chain reaction (PCR) amplified. Gibson assembly (***Gibson et al., 2009***) was used to insert the genes into pEL_A or pEL_K vectors with either N-terminal 6XHis-TEV or 6XHis-GST-TEV tags. Mutations were introduced by PCR of the corresponding plasmids. Plasmids were transformed into *E. coli* BL21 (DE3) and the cells were grown at 37 °C in TB medium supplemented with appropriate antibiotics to an OD_{600} of 1. After cooling down the culture to 18 °C, protein expression was induced by the addition of 0.5 mM Isopropyl β-d-1-thiogalactopyranoside (IPTG). Cells were harvested after overnight protein induction at 18 °C.

Protein purification

Cell pellets were resuspended in four times the pellet volumes of lysis buffer (50 mM Tris pH 7.5, 300 mM NaCl, 10% glycerol, 5 mM β-mercaptoethanol) supplemented with 1 mM phenylmethanesulfonyl fluoride (PMSF) and SM DNAse. The cells were lysed by sonication and clarified by ultracentrifugation at 74,000 relative centrifugal force (RCF) for 30 min. The cleared lysate was loaded onto a Ni^{2+}-NTA column (5 ml, Roche) prewashed with lysis buffer. After loading the lysate, the column was further washed with 8 column volumes (CV) of lysis buffer, 8 CV QB buffer (20 mM Tris pH 7.5, 1 M NaCl, 10% glycerol, 5 mM β-mercaptoethanol), and 8 CV of QA buffer (20 mM Tris pH 7.5, 50 mM NaCl, 10% glycerol, 5 mM β-mercaptoethanol) supplemented with 20 mM imidazole. The proteins were eluted from the Ni^{2+}-NTA column by passing QA buffer containing 250 mM imidazole. The eluted proteins were loaded onto a HiTrap Q HP 5 ml anion exchange column (GE Healthcare) pre-equilibrated with QA buffer. Elution from the Q column was performed by a 0–100% gradient from QA to QB buffer. The elutions containing the proteins were loaded onto a HiLoad 16/600 Superdex 75 or HiLoad 16/600 Superdex 200 column (GE Healthcare) pre-equilibrated with SEC buffer (10 mM HEPES pH 7.5, 150 mM NaCl, 1 mM dithiothreitol [DTT]).

For the purification of His-GST-TEV-$HsIFT172_{1681\text{-}C}$, His-MmUbe1, His-TEV-HsUbcH5a, His-TEV-(Tetra-ubiquitin) and His-Strep-TEV-HsUbiquitin, the cell lysates overexpressing the proteins were prepared as above. After loading the clarified lysate onto the Ni^{2+}-NTA column, the column was washed with 8 CV of lysis buffer, 8 CV of QB buffer, and 8 CV of QA2 buffer (20 mM Tris pH 7.5, 100 mM NaCl, 10% glycerol, 5 mM β-mercaptoethanol) supplemented with 20 mM imidazole. Proteins were eluted by passing 20 mL QA2 buffer containing 250 mM imidazole followed by 20 mL of QA2 buffer containing 500 mM imidazole. The purest elutions were dialyzed overnight in SEC buffer and afterwards loaded on a HiLoad 16/600 Superdex 75 or HiLoad 16/600 Superdex 200 column (GE Healthcare) pre-equilibrated with SEC buffer. Selenomethionine substituted HsIFT172C2 protein was expressed in BL21 Star cells and grown in M9 medium with the addition of amino acids. The protein was purified as described above.

Culturing and flagella isolation of Cr

CrCC-1690 strain was obtained from the Chlamydomonas Resource Center (https://www.chlamycollection.org). The cells were maintained on solid agar plates consisting of standard tris acetate phosphate (TAP) media in a sterile environment at room temperature with a table lamp as a continuous light source. Cells for flagella extraction were grown in two flasks each with 4 L of (TAP) media for 3 days at room temperature with a table lamp as a continuous light source. Cells were grown to an OD_{700} of 0.4. The cultures were harvested and dibucaine-induced flagella abscission and subsequent flagella isolation were carried out as reported in ***Craige et al., 2013***. The isolated flagella were solubilized overnight at 4 °C in solubilization buffer (10 mM HEPES pH 7.5, 5 mM $MgSO_4$, 4% sucrose, 25 mM KCl, 10 mM β-mercaptoethanol, 0.3% IGEPAL 630) supplemented with protease inhibitor (Roche #05892791001). Afterwards, the axonemal fraction of the flagella lysate was pelleted by centrifugation of the flagella lysate at 45,000 RCF for 30 min at 4 °C. The supernatant containing the IFT proteins and motor proteins was used for subsequent pull-downs with $CrIFT172_{968\text{-}C}$.

Affinity pull-down

For the pull-down with *C. reinhardtii* flagella extracts, 30 μM of His-$crIFT172_{968\text{-}C}$ or 30 μM His-TEV protease were immobilized on 50 μL of TALON beads (GE healthcare #28-9574-99) by incubation at

4 °C for 1 hr. Afterwards, the beads were washed three times with HMSK buffer (10 mM HEPES pH 7.4, 5 mM $MgSO_4$, 4%(w/v) sucrose, and 25 mM KCl) to remove unbound proteins. 1 mg *C. reinhardtii* flagella extract diluted in 300 µL HMSK buffer was incubated with the beads at 4 °C for 2 hr. After incubation, the beads were washed three times with HMSK buffer containing 30 mM imidazole, and bound proteins were eluted in HMSK buffer containing 300 mM imidazole.

For the GST pull-down, 10 µM of the GST-tagged protein or GST tag were immobilized on 10 µL GSH beads (Cytiva #17-5279-01) by incubation for 1 hr at 4 °C with constant mixing. Beads were washed once with pull-down buffer (50 mM Tris pH 7.5, 100 mM NaCl, and 1 mM DTT) to remove unbound proteins. Prey proteins were diluted in 100 µL pull-down buffer and incubated with the beads at 4 °C for 2 hr. The beads were washed three times with pull-down buffer, and bound proteins were eluted in elution buffer (10 mM HEPES pH 7.5, 100 mM NaCl, 30 mM reduced glutathione, and 1 mM DTT). The specific amount of prey proteins supplied was 20 µM UbcH5a~Ub in the pull-down shown in ***Figure 4A***, 25 µM tetra-ubiquitin in the pull-down shown in ***Figure 4D***. For the pull-down shown in ***Figure 4C***, 5 µM of immobilized GST-HsIFT172C2 was incubated with 15 µM or 25 µM tetra-ubiquitin as specified. Pull-down elutions were visualized by Coomassie staining and western blotting with anti-ubiquitin (Merck, #05–944, 1:5000) antibody after separation on an SDS-PAGE gel.

Ubiquitination assays

Ubiquitination assays with purified UbcH5a as E2 were performed in a 50 µL reaction volume. The reaction contained 0.1 µM E1 (His-MmUbe1), 2.5 µM E2 (His-TEV-UbcH5a), 10 µM ubiquitin (R&D Systems #U-100H-10M), and 2 µM of the specified His-TEV-HsIFT172C constructs. Reactions were initiated by the addition of 5 mM ATP and incubated at 37 °C for 1.5 hr in ubiquitination buffer (50 mM Tris pH 7.5, 50 mM NaCl, 5 mM $MgCl_2$ and 0.5 mM DTT). The reactions were stopped by addition of equal volumes of 2 X SDS-PAGE loading buffer (100 mM Tris pH 6.8, 10% v/v β-mercaptoethanol, 4% v/v SDS, 0.2% v/v bromophenol blue, 20% v/v glycerol). Reactions were later visualized by Coomassie staining and western blotting with anti-ubiquitin (Merck, #05–944, 1:5000) antibody or anti-His (GeneScript, #A00186, 1:5000) antibody after separation on an 8% SDS-PAGE gel.

For the E2 enzyme screen shown in ***Figure 3B*** and 20 µL reactions were set up containing 0.25 µM E1 (His-MmUbe1), 2.5 µM of the specified E2 enzyme (Abcam #ab139472), 5 µM ubiquitin (R&D Systems #U-100H-10M), and 2 µM His-TEV-HsIFT172C1. The reactions were initiated by addition of 5 mM ATP and carried out in ubiquitination buffer (Abcam #ab139472) supplemented with 5 mM $MgCl_2$. The reactions were incubated at 37 °C for 1.5 hr. The reaction was stopped by addition of equal volumes of 2 X non-reducing SDS-PAGE loading buffer (Abcam #ab139472). Reactions were analyzed by Coomassie staining and western blotting with anti-ubiquitin antibody (Merck, #05–944, 1:5000) after separation on a 4–15% gradient SDS-PAGE gel.

The protocol for generating the UbcH5aC85S~Ub conjugate (***Figure 4—figure supplement 1C***) was adapted from ***Middleton et al., 2014***. Briefly, a 5 mL in vitro charging reaction was set up containing MmUbe1, $UbcH5a_{C85S}$, ubiquitin (recombinantly purified with an N-terminal 6XHis-Strep-TEV tag), and ATP. The charging reaction was incubated overnight at 30 °C to achieve maximal UbcH5aC85S~Ub formation, followed by separation on a HiLoad Superdex 75 SEC column.

Cell culture

Adherent hTERT-immortalized Retinal Pigment Epithelial 1 (RPE1) cells were grown in Dulbecco's Modified Eagle Medium F12 (DMEM/F-12, GlutaMAX Supplement [Gibco #31331–093]) containing 1% penicillin-streptomycin (Sigma-Aldrich #P0781) and 10% fetal bovine serum (FBS, Gibco #10438–026) at 37 °C, 5% CO_2, and 95% humidity. Cells were passaged twice a week. Cells were serum starved for 48 hr prior to ligand stimulation by replacing the culture media with DMEM F12 containing 1% Penicillin-Streptomycin.

Ligand stimulation assays

Serum-starved RPE1 cells were stimulated by addition of respective serum starvation media containing 2 ng/mL TGF-β1 ligand (R&D Systems #240B) for the specified time points. The stimulation was quenched by washing the cells with ice-cold PBS (137 mM NaCl, 2.7 mM KCl, 10 mM Na_2HPO_4, and 1.8 mM KH_2PO_4) followed by addition of lysis buffer. M-Per Lysis buffer (ThermoScientific #78501) supplemented with protease inhibitor (Merck #05056489001) and anti-phosphatase (Thermo Fisher

Table 2. List of primary and secondary antibodies used in western blots.

Protein	Primary antibody catalogue No.	Primary antibody dilution	Secondary antibody catalogue No.	Secondary antibody dilution
ubiquitin	Merck #05–944	1:5000	Dako #P0161	1:1000
His tag	Genscript #A00186	1:5000	Dako #P0161	1:1000
IFT172	Santa Cruz #Sc398393	1:200	Agilent #P0447	1:10,000
p-SMAD2	Cell Signaling #3108 s	1:500	Agilent #P0399	1:10,000
p-AKT^{T308}	Cell Signaling #2965 s	1:500	Agilent #P0399	1:10,000
p-AKT^{S473}	Cell Signaling #4060 s	1:500	Agilent #P0399	1:10,000
SMAD2	Cell Signaling #5339 s	1:200	Agilent #P0399	1:10,000
AKT	Cell Signaling #9272 s	1:500	Agilent #P0399	1:10,000
DCTN1	BD Transduction Laboratories #610474	1:500	Agilent #P0447	1:10,000
GAPDH	Cell Signaling #14 C10	1:1000	Agilent #P0399	1:10,000

Scientific #1862495) was used for quenching and cell lysis. Lysates were centrifuged at 20000 RCF for 20 min at 4 °C and the supernatant was stored at –20 °C. Samples were later analyzed by western blots with antibodies as indicated. Antibodies used in western blots are listed in ***Table 2***.

Crystallization, X-ray diffraction data processing, and structure determination

HsIFT172C2 was crystallized by vapor diffusion by mixing 200 nL of purified protein at a concentration of 2.4 mg/ml mixed with an equal volume of precipitant solution containing 0.2 M sodium phosphate dibasic dihydrate, 20% w/v polyethylene glycol 3350, pH 9.1. Crystals were transferred to the cryo-protectant containing the precipitant solution supplemented with 10% glycerol before freezing. X-ray diffraction data were collected at the Swiss Light Source (SLS; Villigen, Switzerland) at the PXII beam-line on a Pilatus 6 M detector and indexed/integrated with the XDS package (***Kabsch, 2010***) before scaling with Aimless as part of the CCP4 package (***Winn et al., 2011***). Molecular replacement using the AlphaFold generated model for HsIFT172C2 was carried out in the program Phaser (***McCoy et al., 2007***) as available in the software packages PHENIX (***Liebschner et al., 2019***). Molecular replacement identified two molecules of HsIFT172$_{1470\text{-}C}$ in the asymmetric unit. Single anomalous dispersion diffraction data collected at the selenium peak wavelength on selenium methionine substituted protein crystals were combined with the molecular replacement solution in Phaser to produce phase information to calculate the map shown in ***Figure 2—figure supplement 1B***. Given this map, the AutoBuild function in PHENIX was utilized for model building yielding initial R_{work}/R_{free} values of 0.30/0.35. This was followed by iterative cycles of manual model building in Coot (***Raman et al., 2015***) and refinement in PHENIX using torsion angle non-crystallographic symmetry and secondary structure restraints as well as translation libration screw (TLS) refinement, to yield a final model with an R_{work}/R_{free} of 0.195/0.240 (see ***Table 1***).

Mass-spectrometry-based fragment identification for CrIFT172$_{968\text{-}C}$ interactors

Samples were prepared using the SP3 protocol (***Hughes et al., 2019***) with reduction, alkylation, and trypsin digestion. Peptides were labeled with TMT6plex (ThermoFisher) and fractionated by high pH reverse phase chromatography. LC-MS/MS analysis was performed on an UltiMate 3000 RSLC

nano LC system coupled to an Orbitrap Fusion Lumos Tribrid Mass Spectrometer. Full scan MS1 (375–1500 m/z) was acquired at 60,000 resolution, followed by data-dependent MS2 scans at 15,000 resolution. Data were processed using IsobarQuant and Mascot (v2.2.07) against the *C. reinhardtii* proteome (UP000006906). Fixed modifications were carbamidomethyl (C) and TMT10 (K); variable modifications were acetyl (protein N-term), oxidation (M), and TMT10 (N-term). Mass tolerances were 10 ppm for MS1 and 0.02 Da for MS2. Quantification required at least two unique peptides per protein. Data analysis was performed in R, using limma for batch correction and vsn for normalization. Differential expression was assessed using limma, with hits defined as having FDR <5% and fold-change≥100%, and candidates as FDR < 20% and fold-change≥50%.

CRISPR-mediated endogenous tagging of IFT172 in RPE1 cells

The CRISPR/Cas12a-assisted PCR tagging approach was used to endogenously tag IFT172 with eGFP in the RPE1 cell line as previously described (***Kuhns et al., 2024***). Briefly, HDR repair templates were produced by PCR with target-specific primers containing the homology arms and the plasmid pMaCTag-P05 (Addgene plasmid 120016; ***Fueller et al., 2020***). In addition to the homology arms and the eGFP sequence, the HDR repair template also encodes a puromycin cassette for selection and an expression cassette for a Cas12a crRNA. For tagging full-length IFT172 (IFT172-FL) at its C-terminus, the Cas12a crRNA (5′-CCTTTCAGTAGTTGGTAGAG-3′) targeted the IFT172 locus at the stop codon, and the homology arms were designed to insert the eGFP sequence before the stop codon. To generate the deletion of the IFT172 U-box domain (IFT172 ΔU-box), the homology arms were designed to insert the eGFP sequence after amino acid 1688, and the target sequence of the corresponding Cas12a crRNA (5′-TTACAGGTATAGAAGCCTAC-3′) spanned the intended integration site. Doxycycline-inducible RPE1 cells expressing the CRISPR nuclease enAsCas12a (***Kleinstiver et al., 2019***) were electroporated with the HDR repair template using the Neon Transfection System (Thermo Fisher Scientific). After the transfection, the cells were treated for three days with the DNA-PK inhibitor M3814 to increase the knock-in efficiency (***Riesenberg et al., 2019***) and subsequently selected with puromycin for 2 weeks to isolate single-cell clones. The clonal cell lines were screened for successful tagging by live cell imaging and PCR. In this study, four cell lines were used (***Figure 5A***). 1: IFT172-FL (homozygous): Both alleles contained the eGFP insert at the C-terminus before the stop codon. 2: IFT172-FL (heterozygous): One allele contained the eGFP insert at the C-terminus; the other allele was the unaltered wildtype allele. 3: IFT172 ΔU-box (homozygous): U-box domain deleted in both alleles by the insertion of eGFP after amino acid 1688. 4: IFT172 ΔU-box (heterozygous): U-box domain deleted in one allele; the other allele was the unaltered wildtype allele. Correct knock-in and the absence of indels were confirmed by Sanger sequencing.

Immunofluorescence staining and microscopy

RPE1 cells were grown on glass coverslips to 70–80% confluency and serum-starved for 24 hr to induce ciliogenesis. Cells were fixed with 3% PFA in PBS for 15 min and permeabilized for 5 min in 0.2% Triton X-100/PBS. Blocking was performed for 30 min with 3% BSA in PBS. A mouse monoclonal antibody against acetylated tubulin (Sigma-Aldrich, Clone 6-11B-1, diluted 1:500) was used to stain for the ciliary axoneme. For protein localization studies, GFP fluorescence was visualized directly. Primary antibodies were diluted in blocking solution and incubated with the cells at room temperature for 2 hr or at 4 °C overnight. Coverslips were washed three times with PBS and incubated with an anti-mouse secondary antibody conjugated to Cy3 (Jackson Immuno Research Labs, Cat# 715-165-150, diluted 1:500) for 1 hr at room temperature. DAPI (40,6-diamidino-2-phenylindole, Sigma-Aldrich) was included with secondary antibodies for DNA staining. Coverslips were washed three times with PBS and mounted on glass slides in Mowiol (Sigma-Aldrich).

Widefield images were acquired as z-stacks at 0.3 µm intervals using a Zeiss AxioImager M1 microscope equipped with a Zeiss CellObserver equipped with an Apochromat 63×/NA1.4 oil-immersion objective and a CoolSNAP HQ2 camera. Confocal images were acquired as z-stacks at 0.125 µm intervals using a Nikon Ti-2, A1 LFO confocal microscope with a Plan Apo λ 100×NA 1.4 oil objective. Image analysis was performed using Fiji/ImageJ (NIH; ***Schindelin et al., 2012***). For quantification of ciliation frequencies, maximum intensity projections of z-stacks were generated, and the number of nuclei/cells and cilia were determined using DAPI and acetylated tubulin staining, respectively. For ciliary length measurements, the region of interest was manually defined using the line segment tool.

Measurements were obtained from four independent experiments, and 30–60 cells were analyzed per condition and replicate. Graphs were drawn, and statistical analysis was performed using Prism (GraphPad). Data are presented as mean ± SEM or box-and-whisker plots with horizontal lines showing 25, 50, and 75th percentiles and whiskers extending to minimum and maximum values.

AlphaFold

All structural models not supported by crystallographic data were predicted using a local installation of AlphaFold v. 2.3.2 (***Jumper et al., 2021***; ***Evans, 2021***). Visualizations of protein structure were done using PyMOL v. 2.5 (Schrodinger LLC, https://pymol.org).

Acknowledgements

We thank Jesper L Karlsen and Rune T Kidmose for assistance with biocomputing and the Institute of Molecular Biology and Genetics at Aarhus University for computing time. We also thank Michael Knop, Keith Joung, and Benjamin Kleinstiver for reagents and the Danish Molecular Biomedical Imaging Center, University of Southern Denmark, for the use of imaging equipment, supported by Novo Nordisk Foundation (NNF18SA0032928). This work was funded by grants from the Novo Nordisk Foundation (grant numbers NNF15OC00114164 and NNF23OC0085823) and the European Union's Horizon 2020 research and innovation program Marie Sklodowska-Curie Innovative Training Networks (ITN) grant 861329 to EL.

Additional information

Funding

Funder	Grant reference number	Author
Novo Nordisk Fonden	NNF23OC0085823	Esben Lorentzen
Novo Nordisk Fonden	NNF15OC00114164	Esben Lorentzen
Horizon 2020 Framework Programme	10.3030/861329	Esben Lorentzen
Novo Nordisk Fonden	NNF18SA0032928	Jens S Andersen

The funders had no role in study design, data collection and interpretation, or the decision to submit the work for publication.

Author contributions

Nevin K Zacharia, Conceptualization, Data curation, Formal analysis, Validation, Investigation, Visualization, Methodology, Writing - original draft, Writing - review and editing; Stefanie Kuhns, Formal analysis, Validation, Investigation, Methodology; Niels Boegholm, Jiaolong Wang, Lucie Menguy, Investigation, Methodology; Anni Christensen, Methodology; Narcis A Petriman, Conceptualization, Supervision, Validation, Investigation, Methodology; Anna Lorentzen, Conceptualization, Formal analysis, Supervision, Validation, Investigation, Methodology; Jindriska L Fialova, Formal analysis, Supervision, Investigation, Methodology; Sophie Saunier, Conceptualization, Supervision; Søren Tvorup Christensen, Conceptualization, Supervision, Writing - original draft, Project administration, Writing - review and editing; Jens S Andersen, Supervision, Project administration; Sagar Bhogaraju, Conceptualization, Formal analysis, Supervision, Investigation, Methodology, Writing - original draft, Project administration, Writing - review and editing; Esben Lorentzen, Conceptualization, Data curation, Formal analysis, Supervision, Funding acquisition, Validation, Visualization, Writing - original draft, Project administration, Writing - review and editing

Author ORCIDs

Nevin K Zacharia https://orcid.org/0000-0003-2613-2610
Stefanie Kuhns https://orcid.org/0000-0002-3065-7818
Narcis A Petriman https://orcid.org/0000-0002-3189-7530
Anna Lorentzen https://orcid.org/0000-0002-4405-935X

Søren Tvorup Christensen https://orcid.org/0000-0001-5004-304X
Sagar Bhogaraju https://orcid.org/0000-0001-9998-5927
Esben Lorentzen https://orcid.org/0000-0001-6493-7220

Peer review material
Reviewer #1 (Public review): https://doi.org/10.7554/eLife.104906.3.sa1
Reviewer #2 (Public review): https://doi.org/10.7554/eLife.104906.3.sa2
Reviewer #3 (Public review): https://doi.org/10.7554/eLife.104906.3.sa3
Author response https://doi.org/10.7554/eLife.104906.3.sa4

Additional files

Supplementary files

MDAR checklist

Data availability

Atomic coordinates and structure factors for the HsIFT172 C-terminal domain crystal structure have been deposited in the Protein Data Bank under accession code 9H2D. The mass spectrometry proteomics data have been deposited to the ProteomeXchange Consortium via the PRIDE partner repository with the dataset identifier PXD078483. All other data supporting the findings of this study are available within the article and its supplementary materials.

The following datasets were generated:

Author(s)	Year	Dataset title	Dataset URL	Database and Identifier
Stein F, Bhogaraju S	2026	IFT172 C-term interactome in chlamydomonas flagella extracts	https://www.ebi.ac.uk/pride/archive/projects/PXD078483	PRIDE, PXD078483
Lorentzen E, Zacharia NK, Bhogaraju S	2024	Human IFT172 C-terminal U-box domain crystal structure	https://doi.org/10.2210/pdb9h2d/pdb	Worldwide Protein Data Bank, 10.2210/pdb9h2d/pdb

References

Aravind L, Koonin EV. 2000. The U box is a modified RING finger - a common domain in ubiquitination. *Current Biology* **10**:R132–R134. DOI: https://doi.org/10.1016/s0960-9822(00)00398-5, PMID: 10704423

Aslanyan MG, Doornbos C, Diwan GD, Anvarian Z, Beyer T, Junger K, van Beersum SEC, Russell RB, Ueffing M, Ludwig A, Boldt K, Pedersen LB, Roepman R. 2023. A targeted multi-proteomics approach generates a blueprint of the ciliary ubiquitinome. *Frontiers in Cell and Developmental Biology* **11**:1113656. DOI: https://doi.org/10.3389/fcell.2023.1113656, PMID: 36776558

Bhogaraju S, Weber K, Engel BD, Lechtreck KF, Lorentzen E. 2014. Getting tubulin to the tip of the cilium: one IFT train, many different tubulin cargo-binding sites? *BioEssays* **36**:463–467. DOI: https://doi.org/10.1002/bies.201400007, PMID: 24616010

Bomar MG, Pai MT, Tzeng SR, Li SSC, Zhou P. 2007. Structure of the ubiquitin-binding zinc finger domain of human DNA Y-polymerase eta. *EMBO Reports* **8**:247–251. DOI: https://doi.org/10.1038/sj.embor.7400901, PMID: 17304240

Buetow L, Huang DT. 2016. Structural insights into the catalysis and regulation of E3 ubiquitin ligases. *Nature Reviews. Molecular Cell Biology* **17**:626–642. DOI: https://doi.org/10.1038/nrm.2016.91, PMID: 27485899

Bujakowska KM, Zhang Q, Siemiatkowska AM, Liu Q, Place E, Falk MJ, Consugar M, Lancelot M-E, Antonio A, Lonjou C, Carpentier W, Mohand-Saïd S, den Hollander AI, Cremers FPM, Leroy BP, Gai X, Sahel J-A, van den Born LI, Collin RWJ, Zeitz C, et al. 2015. Mutations in IFT172 cause isolated retinal degeneration and Bardet-Biedl syndrome. *Human Molecular Genetics* **24**:230–242. DOI: https://doi.org/10.1093/hmg/ddu441, PMID: 25168386

Chiuso F, Delle Donne R, Giamundo G, Rinaldi L, Borzacchiello D, Moraca F, Intartaglia D, Iannucci R, Senatore E, Lignitto L, Garbi C, Conflitti P, Catalanotti B, Conte I, Feliciello A. 2023. Ubiquitylation of BBSome is required for ciliary assembly and signaling. *EMBO Reports* **24**:e55571. DOI: https://doi.org/10.15252/embr.202255571, PMID: 36744302

Clement CA, Ajbro KD, Koefoed K, Vestergaard ML, Veland IR, Henriques de Jesus MPR, Pedersen LB, Benmerah A, Andersen CY, Larsen LA, Christensen ST. 2013. TGF-β signaling is associated with endocytosis at the pocket region of the primary cilium. *Cell Reports* **3**:1806–1814. DOI: https://doi.org/10.1016/j.celrep.2013.05.020, PMID: 23746451

Craige B, Brown JM, Witman GB. 2013. Isolation of Chlamydomonas flagella. *Current Protocols in Cell Biology* **Chapter 3**:3. DOI: https://doi.org/10.1002/0471143030.cb0341s59, PMID: 23728744
de Bie P, Ciechanover A. 2011. Ubiquitination of E3 ligases: self-regulation of the ubiquitin system via proteolytic and non-proteolytic mechanisms. *Cell Death and Differentiation* **18**:1393–1402. DOI: https://doi.org/10.1038/cdd.2011.16, PMID: 21372847
de Moura TR, Mozaffari-Jovin S, Szabó CZK, Schmitzová J, Dybkov O, Cretu C, Kachala M, Svergun D, Urlaub H, Lührmann R, Pena V. 2018. Prp19/Pso4 is an autoinhibited ubiquitin ligase activated by stepwise assembly of three splicing factors. *Molecular Cell* **69**:979–992.. DOI: https://doi.org/10.1016/j.molcel.2018.02.022
Desai PB, Stuck MW, Lv B, Pazour GJ. 2020. Ubiquitin links smoothened to intraflagellar transport to regulate Hedgehog signaling. *The Journal of Cell Biology* **219**:e201912104. DOI: https://doi.org/10.1083/jcb.201912104, PMID: 32435793
Doganli C. 2024. TAK1 operates at the primary cilium in non-canonical tgfb/bmp signaling to control heart development. *bioRxiv*. DOI: https://doi.org/10.1101/2024.05.06.592628
Dou H, Buetow L, Hock A, Sibbet GJ, Vousden KH, Huang DT. 2012a. Structural basis for autoinhibition and phosphorylation-dependent activation of c-Cbl. *Nature Structural & Molecular Biology* **19**:184–192. DOI: https://doi.org/10.1038/nsmb.2231
Dou H, Buetow L, Sibbet GJ, Cameron K, Huang DT. 2012b. BIRC7-E2 ubiquitin conjugate structure reveals the mechanism of ubiquitin transfer by a RING dimer. *Nature Structural & Molecular Biology* **19**:876–883. DOI: https://doi.org/10.1038/nsmb.2379, PMID: 22902369
Eguether T, San Agustin JT, Keady BT, Jonassen JA, Liang Y, Francis R, Tobita K, Johnson CA, Abdelhamed ZA, Lo CW, Pazour GJ. 2014. IFT27 links the BBSome to IFT for maintenance of the ciliary signaling compartment. *Developmental Cell* **31**:279–290. DOI: https://doi.org/10.1016/j.devcel.2014.09.011, PMID: 25446516
Evans R. 2021. Protein complex prediction with alphafold-multimer. *bioRxiv*. DOI: https://doi.org/10.1101/2021.10.04.463034
Focșa IO, Budișteanu M, Bălgrădean M. 2021. Clinical and genetic heterogeneity of primary ciliopathies (Review). *International Journal of Molecular Medicine* **48**:176. DOI: https://doi.org/10.3892/ijmm.2021.5009, PMID: 34278440
Fueller J, Herbst K, Meurer M, Gubicza K, Kurtulmus B, Knopf JD, Kirrmaier D, Buchmuller BC, Pereira G, Lemberg MK, Knop M. 2020. CRISPR-Cas12a-assisted PCR tagging of mammalian genes. *The Journal of Cell Biology* **219**:e201910210. DOI: https://doi.org/10.1083/jcb.201910210, PMID: 32406907
Garcia-Barcena C, Osinalde N, Ramirez J, Mayor U. 2020. How to inactivate human ubiquitin E3 ligases by mutation. *Frontiers in Cell and Developmental Biology* **8**:39. DOI: https://doi.org/10.3389/fcell.2020.00039, PMID: 32117970
Gibson DG, Young L, Chuang RY, Venter JC, Hutchison CA, Smith HO. 2009. Enzymatic assembly of DNA molecules up to several hundred kilobases. *Nature Methods* **6**:343–345. DOI: https://doi.org/10.1038/nmeth.1318, PMID: 19363495
Gundogdu M, Walden H. 2019. Structural basis of generic versus specific E2-RING E3 interactions in protein ubiquitination. *Protein Science* **28**:1758–1770. DOI: https://doi.org/10.1002/pro.3690, PMID: 31340062
Guo X, Wang XF. 2009. Signaling cross-talk between TGF-beta/BMP and other pathways. *Cell Research* **19**:71–88. DOI: https://doi.org/10.1038/cr.2008.302, PMID: 19002158
Halbritter J, Bizet AA, Schmidts M, Porath JD, Braun DA, Gee HY, Mclnerney-Leo AM, Krug P, Filhol E, Davis EE, Airik R, Czarnecki PG, Lehman AM, Trnka P, Nitschké P, Bole-Feysot C, Schueler M, Knebelmann B, Burtey S, Szabó AJ, et al. 2013. Defects in the IFT-B component IFT172 cause Jeune and Mainzer-Saldino syndromes in humans. *American Journal of Human Genetics* **93**:915–925. DOI: https://doi.org/10.1016/j.ajhg.2013.09.012, PMID: 24140113
Hatakeyama S, Yada M, Matsumoto M, Ishida N, Nakayama KI. 2001. U box proteins as a new family of ubiquitin-protein ligases. *The Journal of Biological Chemistry* **276**:33111–33120. DOI: https://doi.org/10.1074/jbc.M102755200, PMID: 11435423
Heldin CH, Moustakas A. 2016. Signaling receptors for TGF-β family members. *Cold Spring Harbor Perspectives in Biology* **8**:a022053. DOI: https://doi.org/10.1101/cshperspect.a022053, PMID: 27481709
Hoeller D, Hecker C-M, Wagner S, Rogov V, Dötsch V, Dikic I. 2007. E3-independent monoubiquitination of ubiquitin-binding proteins. *Molecular Cell* **26**:891–898. DOI: https://doi.org/10.1016/j.molcel.2007.05.014, PMID: 17588522
Holm L. 2020. Using Dali for Protein Structure Comparison. *Methods in Molecular Biology* **2112**:29–42. DOI: https://doi.org/10.1007/978-1-0716-0270-6_3, PMID: 32006276
Hornbeck PV, Zhang B, Murray B, Kornhauser JM, Latham V, Skrzypek E. 2015. PhosphoSitePlus, 2014: mutations, PTMs and recalibrations. *Nucleic Acids Research* **43**:D512–D520. DOI: https://doi.org/10.1093/nar/gku1267, PMID: 25514926
Hossain D, Tsang WY. 2019. The role of ubiquitination in the regulation of primary cilia assembly and disassembly. *Seminars in Cell & Developmental Biology* **93**:145–152. DOI: https://doi.org/10.1016/j.semcdb.2018.09.005, PMID: 30213760
Huang K, Diener DR, Rosenbaum JL. 2009. The ubiquitin conjugation system is involved in the disassembly of cilia and flagella. *The Journal of Cell Biology* **186**:601–613. DOI: https://doi.org/10.1083/jcb.200903066, PMID: 19704024
Huangfu D, Liu A, Rakeman AS, Murcia NS, Niswander L, Anderson KV. 2003. Hedgehog signalling in the mouse requires intraflagellar transport proteins. *Nature* **426**:83–87. DOI: https://doi.org/10.1038/nature02061, PMID: 14603322

Hughes CS, Moggridge S, Müller T, Sorensen PH, Morin GB, Krijgsveld J. 2019. Single-pot, solid-phase-enhanced sample preparation for proteomics experiments. *Nature Protocols* **14**:68–85. DOI: https://doi.org/10.1038/s41596-018-0082-x, PMID: 30464214

Jiang M, Palicharla VR, Miller D, Hwang S-H, Zhu H, Hixson P, Mukhopadhyay S, Sun J. 2023. Human IFT-A complex structures provide molecular insights into ciliary transport. *Cell Research* **33**:288–298. DOI: https://doi.org/10.1038/s41422-023-00778-3, PMID: 36775821

Jordan MA, Diener DR, Stepanek L, Pigino G. 2018. The cryo-EM structure of intraflagellar transport trains reveals how dynein is inactivated to ensure unidirectional anterograde movement in cilia. *Nature Cell Biology* **20**:1250–1255. DOI: https://doi.org/10.1038/s41556-018-0213-1, PMID: 30323187

Jumper J, Evans R, Pritzel A, Green T, Figurnov M, Ronneberger O, Tunyasuvunakool K, Bates R, Žídek A, Potapenko A, Bridgland A, Meyer C, Kohl SAA, Ballard AJ, Cowie A, Romera-Paredes B, Nikolov S, Jain R, Adler J, Back T, et al. 2021. Highly accurate protein structure prediction with AlphaFold. *Nature* **596**:583–589. DOI: https://doi.org/10.1038/s41586-021-03819-2

Kabsch W. 2010. Acta Crystallogr. *D Biol. Crystallog* **66**:125–132. DOI: https://doi.org/10.1107/S0907444909047337

Kassenbrock CK, Anderson SM. 2004. Regulation of ubiquitin protein ligase activity in c-Cbl by phosphorylation-induced conformational change and constitutive activation by tyrosine to glutamate point mutations. *The Journal of Biological Chemistry* **279**:28017–28027. DOI: https://doi.org/10.1074/jbc.M404114200, PMID: 15117950

Kim J, Hsia EYC, Brigui A, Plessis A, Beachy PA, Zheng X. 2015. The role of ciliary trafficking in Hedgehog receptor signaling. *Science Signaling* **8**:ra55. DOI: https://doi.org/10.1126/scisignal.aaa5622, PMID: 26038600

Kleinstiver BP, Sousa AA, Walton RT, Tak YE, Hsu JY, Clement K, Welch MM, Horng JE, Malagon-Lopez J, Scarfò I, Maus MV, Pinello L, Aryee MJ, Joung JK. 2019. Engineered CRISPR-Cas12a variants with increased activities and improved targeting ranges for gene, epigenetic and base editing. *Nature Biotechnology* **37**:276–282. DOI: https://doi.org/10.1038/s41587-018-0011-0, PMID: 30742127

Kloppsteck P, Ewens CA, Förster A, Zhang X, Freemont PS. 2012. Regulation of p97 in the ubiquitin–proteasome system by the UBX protein-family. *Biochimica et Biophysica Acta (BBA) - Molecular Cell Research* **1823**:125–129. DOI: https://doi.org/10.1016/j.bbamcr.2011.09.006

Komander D, Rape M. 2012. The ubiquitin code. *Annual Review of Biochemistry* **81**:203–229. DOI: https://doi.org/10.1146/annurev-biochem-060310-170328, PMID: 22524316

Kozminski KG, Johnson KA, Forscher P, Rosenbaum JL. 1993. A motility in the eukaryotic flagellum unrelated to flagellar beating. *PNAS* **90**:5519–5523. DOI: https://doi.org/10.1073/pnas.90.12.5519

Kozminski KG, Beech PL, Rosenbaum JL. 1995. The Chlamydomonas kinesin-like protein FLA10 is involved in motility associated with the flagellar membrane. *The Journal of Cell Biology* **131**:1517–1527. DOI: https://doi.org/10.1083/jcb.131.6.1517

Kuhns S, Juhl AD, Anvarian Z, Wüstner D, Pedersen LB, Andersen JS. 2024. Endogenous tagging of ciliary genes in human rpe1 cells for live-cell imaging. *Methods in Molecular Biology* **2725**:147–166. DOI: https://doi.org/10.1007/978-1-0716-3507-0_9, PMID: 37856023

Lacey SE, Foster HE, Pigino G. 2023. The molecular structure of IFT-A and IFT-B in anterograde intraflagellar transport trains. *Nature Structural & Molecular Biology* **30**:584–593. DOI: https://doi.org/10.1038/s41594-022-00905-5, PMID: 36593313

Lacey SE, Graziadei A, Pigino G. 2024. Extensive structural rearrangement of intraflagellar transport trains underpins bidirectional cargo transport. *Cell* **187**:4621–4636.. DOI: https://doi.org/10.1016/j.cell.2024.06.041, PMID: 39067443

Lechtreck KF. 2015. IFT–cargo interactions and protein transport in cilia. *Trends in Biochemical Sciences* **40**:765–778. DOI: https://doi.org/10.1016/j.tibs.2015.09.003

Levin I, Eakin C, Blanc M-P, Klevit RE, Miller SI, Brzovic PS. 2010. Identification of an unconventional E3 binding surface on the UbcH5 ~ Ub conjugate recognized by a pathogenic bacterial E3 ligase. *PNAS* **107**:2848–2853. DOI: https://doi.org/10.1073/pnas.0914821107, PMID: 20133640

Liebschner D, Afonine PV, Baker ML, Bunkóczi G, Chen VB, Croll TI, Hintze B, Hung L-W, Jain S, McCoy AJ, Moriarty NW, Oeffner RD, Poon BK, Prisant MG, Read RJ, Richardson JS, Richardson DC, Sammito MD, Sobolev OV, Stockwell DH, et al. 2019. Macromolecular structure determination using X-rays, neutrons and electrons: recent developments in *Phenix*. *Acta Crystallographica Section D Structural Biology* **75**:861–877. DOI: https://doi.org/10.1107/S2059798319011471

Long H, Huang K. 2020. Transport of ciliary membrane proteins. *Frontiers in Cell and Developmental Biology* **7**:00381. DOI: https://doi.org/10.3389/fcell.2019.00381

Lucas-Herald AK, Kinning E, Iida A, Wang Z, Miyake N, Ikegawa S, McNeilly J, Ahmed SF. 2015. A case of functional growth hormone deficiency and early growth retardation in a child with IFT172 mutations. *The Journal of Clinical Endocrinology and Metabolism* **100**:1221–1224. DOI: https://doi.org/10.1210/jc.2014-3852, PMID: 25664603

Lv B, Stuck MW, Desai PB, Cabrera OA, Pazour GJ. 2021. E3 ubiquitin ligase Wwp1 regulates ciliary dynamics of the Hedgehog receptor Smoothened. *The Journal of Cell Biology* **220**:e202010177. DOI: https://doi.org/10.1083/jcb.202010177, PMID: 34161574

McCoy AJ, Grosse-Kunstleve RW, Adams PD, Winn MD, Storoni LC, Read RJ. 2007. Phaser crystallographic software. *Journal of Applied Crystallography* **40**:658–674. DOI: https://doi.org/10.1107/S0021889807021206, PMID: 19461840

Middleton AJ, Budhidarmo R, Day C. 2014. Use of E2~ubiquitin conjugates for the characterization of ubiquitin transfer by RING E3 ligases such as the inhibitor of apoptosis proteins. In: Ashkenazi A, Wells JA, Yuan J (Eds). *Methods in Enzymology*. ScirncceDirect. p. 243–263.

Mill P, Christensen ST, Pedersen LB. 2023. Primary cilia as dynamic and diverse signalling hubs in development and disease. *Nature Reviews. Genetics* **24**:421–441. DOI: https://doi.org/10.1038/s41576-023-00587-9, PMID: 37072495

Mukhopadhyay S, Wen X, Chih B, Nelson CD, Lane WS, Scales SJ, Jackson PK. 2010. TULP3 bridges the IFT-A complex and membrane phosphoinositides to promote trafficking of G protein-coupled receptors into primary cilia. *Genes & Development* **24**:2180–2193. DOI: https://doi.org/10.1101/gad.1966210

Nachury MV, Loktev AV, Zhang Q, Westlake CJ, Peränen J, Merdes A, Slusarski DC, Scheller RH, Bazan JF, Sheffield VC, Jackson PK. 2007. A core complex of BBS proteins cooperates with the GTPase Rab8 to promote ciliary membrane biogenesis. *Cell* **129**:1201–1213. DOI: https://doi.org/10.1016/j.cell.2007.03.053, PMID: 17574030

Nielsen BS, Malinda RR, Schmid FM, Pedersen SF, Christensen ST, Pedersen LB. 2015. PDGFRβ and oncogenic mutant PDGFRα D842V promote disassembly of primary cilia through a PLCγ- and AURKA-dependent mechanism. *Journal of Cell Science* **128**:3543–3549. DOI: https://doi.org/10.1242/jcs.173559, PMID: 26290382

Ohi MD, Vander Kooi CW, Rosenberg JA, Chazin WJ, Gould KL. 2003. Structural insights into the U-box, a domain associated with multi-ubiquitination. *Nature Structural & Molecular Biology* **10**:250–255. DOI: https://doi.org/10.1038/nsb906

Ozkan E, Yu H, Deisenhofer J. 2005. Mechanistic insight into the allosteric activation of a ubiquitin-conjugating enzyme by RING-type ubiquitin ligases. *PNAS* **102**:18890–18895. DOI: https://doi.org/10.1073/pnas.0509418102, PMID: 16365295

Pazour GJ, Dickert BL, Witman GB. 1999. The DHC1b (DHC2) isoform of cytoplasmic dynein is required for flagellar assembly. *The Journal of Cell Biology* **144**:473–481. DOI: https://doi.org/10.1083/jcb.144.3.473

Pedersen LB, Miller MS, Geimer S, Leitch JM, Rosenbaum JL, Cole DG. 2005. Chlamydomonas IFT172 is encoded by FLA11, interacts with CrEB1, and regulates IFT at the flagellar tip. *Current Biology* **15**:262–266. DOI: https://doi.org/10.1016/j.cub.2005.01.037, PMID: 15694311

Pedersen LB, Geimer S, Rosenbaum JL. 2006. Dissecting the molecular mechanisms of intraflagellar transport in chlamydomonas. *Current Biology* **16**:450–459. DOI: https://doi.org/10.1016/j.cub.2006.02.020

Petriman NA, Loureiro-López M, Taschner M, Zacharia NK, Georgieva MM, Boegholm N, Wang J, Mourão A, Russell RB, Andersen JS, Lorentzen E. 2022. Biochemically validated structural model of the 15-subunit intraflagellar transport complex IFT-B. *The EMBO Journal* **41**:e112440. DOI: https://doi.org/10.15252/embj.2022112440, PMID: 36354106

Pigino G, Geimer S, Lanzavecchia S, Paccagnini E, Cantele F, Diener DR, Rosenbaum JL, Lupetti P. 2009. Electron-tomographic analysis of intraflagellar transport particle trains in situ. *The Journal of Cell Biology* **187**:135–148. DOI: https://doi.org/10.1083/jcb.200905103, PMID: 19805633

Plechanovová A, Jaffray EG, Tatham MH, Naismith JH, Hay RT. 2012. Structure of a RING E3 ligase and ubiquitin-loaded E2 primed for catalysis. *Nature* **489**:115–120. DOI: https://doi.org/10.1038/nature11376

Porter ME, Bower R, Knott JA, Byrd P, Dentler W. 1999. Cytoplasmic dynein heavy chain 1b is required for flagellar assembly in *Chlamydomonas* . *Molecular Biology of the Cell* **10**:693–712. DOI: https://doi.org/10.1091/mbc.10.3.693

Pruski M, Hu L, Yang C, Wang Y, Zhang J-B, Zhang L, Huang Y, Rajnicek AM, St Clair D, McCaig CD, Lang B, Ding Y-Q. 2019. Roles for IFT172 and primary cilia in cell migration, cell division, and neocortex development. *Frontiers in Cell and Developmental Biology* **7**:287. DOI: https://doi.org/10.3389/fcell.2019.00287, PMID: 31850339

Raman M, Sergeev M, Garnaas M, Lydeard JR, Huttlin EL, Goessling W, Shah JV, Harper JW. 2015. Systematic proteomics of the VCP-UBXD adaptor network identifies a role for UBXN10 in regulating ciliogenesis. *Nature Cell Biology* **17**:1356–1369. DOI: https://doi.org/10.1038/ncb3238, PMID: 26389662

Reiter JF, Leroux MR. 2017. Genes and molecular pathways underpinning ciliopathies. *Nature Reviews. Molecular Cell Biology* **18**:533–547. DOI: https://doi.org/10.1038/nrm.2017.60, PMID: 28698599

Riesenberg S, Chintalapati M, Macak D, Kanis P, Maricic T, Pääbo S. 2019. Simultaneous precise editing of multiple genes in human cells. *Nucleic Acids Research* **47**:e116. DOI: https://doi.org/10.1093/nar/gkz669, PMID: 31392986

Rosenbaum JL, Witman GB. 2002. Intraflagellar transport. *Nature Reviews Molecular Cell Biology* **3**:813–825. DOI: https://doi.org/10.1038/nrm952

Satir P, Christensen ST. 2007. Overview of structure and function of mammalian cilia. *Annual Review of Physiology* **69**:377–400. DOI: https://doi.org/10.1146/annurev.physiol.69.040705.141236, PMID: 17009929

Schindelin J, Arganda-Carreras I, Frise E, Kaynig V, Longair M, Pietzsch T, Preibisch S, Rueden C, Saalfeld S, Schmid B, Tinevez J-Y, White DJ, Hartenstein V, Eliceiri K, Tomancak P, Cardona A. 2012. Fiji: an open-source platform for biological-image analysis. *Nature Methods* **9**:676–682. DOI: https://doi.org/10.1038/nmeth.2019, PMID: 22743772

Shim MS, Nettesheim A, Dixon A, Liton PB. 2021. Primary cilia and the reciprocal activation of AKT and SMAD2/3 regulate stretch-induced autophagy in trabecular meshwork cells. *PNAS* **118**:e2021942118. DOI: https://doi.org/10.1073/pnas.2021942118, PMID: 33753495

Shinde SR, Nager AR, Nachury MV. 2020. Ubiquitin chains earmark GPCRs for BBSome-mediated removal from cilia. *The Journal of Cell Biology* **219**:e202003020. DOI: https://doi.org/10.1083/jcb.202003020, PMID: 33185668

Shinde SR, Mick DU, Aoki E, Rodrigues RB, Gygi SP, Nachury MV. 2023. The ancestral ESCRT protein TOM1L2 selects ubiquitinated cargoes for retrieval from cilia. *Developmental Cell* **58**:677–693.. DOI: https://doi.org/10.1016/j.devcel.2023.03.003, PMID: 37019113

Soss SE, Klevit RE, Chazin WJ. 2013. Activation of UbcH5c~Ub is the result of a shift in interdomain motions of the conjugate bound to U-Box E3 Ligase E4B. *Biochemistry* **52**:2991–2999. DOI: https://doi.org/10.1021/bi3015949

Taschner M, Lorentzen E. 2016. The intraflagellar transport machinery. *Cold Spring Harbor Perspectives in Biology* **8**:a028092. DOI: https://doi.org/10.1101/cshperspect.a028092, PMID: 27352625

Taschner M, Weber K, Mourão A, Vetter M, Awasthi M, Stiegler M, Bhogaraju S, Lorentzen E. 2016. Intraflagellar transport proteins 172, 80, 57, 54, 38, and 20 form a stable tubulin-binding IFT-B2 complex. *The EMBO Journal* **35**:773–790. DOI: https://doi.org/10.15252/embj.201593164, PMID: 26912722

Trempe J-F, Sauvé V, Grenier K, Seirafi M, Tang MY, Ménade M, Al-Abdul-Wahid S, Krett J, Wong K, Kozlov G, Nagar B, Fon EA, Gehring K. 2013. Structure of parkin reveals mechanisms for ubiquitin ligase activation. *Science* **340**:1451–1455. DOI: https://doi.org/10.1126/science.1237908

Tsao CC, Gorovsky MA. 2008. Different Effects of *Tetrahymena IFT172* domains on anterograde and retrograde intraflagellar Transport . *Molecular Biology of the Cell* **19**:1450–1461. DOI: https://doi.org/10.1091/mbc.e07-05-0403

van den Hoek H, Klena N, Jordan MA, Alvarez Viar G, Righetto RD, Schaffer M, Erdmann PS, Wan W, Geimer S, Plitzko JM, Baumeister W, Pigino G, Hamel V, Guichard P, Engel BD. 2022. In situ architecture of the ciliary base reveals the stepwise assembly of intraflagellar transport trains. *Science* **377**:543–548. DOI: https://doi.org/10.1126/science.abm6704, PMID: 35901159

Walia V, Cuenca A, Vetter M, Insinna C, Perera S, Lu Q, Ritt DA, Semler E, Specht S, Stauffer J, Morrison DK, Lorentzen E, Westlake CJ. 2019. Akt regulates a rab11-effector switch required for ciliogenesis. *Developmental Cell* **50**:229–246. DOI: https://doi.org/10.1016/j.devcel.2019.05.022, PMID: 31204173

Wan KY. 2018. Coordination of eukaryotic cilia and flagella. *Essays in Biochemistry* **62**:829–838. DOI: https://doi.org/10.1042/EBC20180029, PMID: 30464007

Wang Q, Taschner M, Ganzinger KA, Kelley C, Villasenor A, Heymann M, Schwille P, Lorentzen E, Mizuno N. 2018. Membrane association and remodeling by intraflagellar transport protein IFT172. *Nature Communications* **9**:4684. DOI: https://doi.org/10.1038/s41467-018-07037-9

Wang Q, Peng Z, Long H, Deng X, Huang K. 2019. Polyubiquitylation of α-tubulin at K304 is required for flagellar disassembly in *Chlamydomonas*. *Journal of Cell Science* **132**:jcs229047. DOI: https://doi.org/10.1242/jcs.229047, PMID: 30765466

Williamson SM, Silva DA, Richey E, Qin H. 2012. Probing the role of IFT particle complex A and B in flagellar entry and exit of IFT-dynein in Chlamydomonas. *Protoplasma* **249**:851–856. DOI: https://doi.org/10.1007/s00709-011-0311-4, PMID: 21853389

Wingfield JL, Mengoni I, Bomberger H, Jiang Y-Y, Walsh JD, Brown JM, Picariello T, Cochran DA, Zhu B, Pan J, Eggenschwiler J, Gaertig J, Witman GB, Kner P, Lechtreck K. 2017. IFT trains in different stages of assembly queue at the ciliary base for consecutive release into the cilium. *eLife* **6**:e26609. DOI: https://doi.org/10.7554/eLife.26609, PMID: 28562242

Winn MD, Ballard CC, Cowtan KD, Dodson EJ, Emsley P, Evans PR, Keegan RM, Krissinel EB, Leslie AGW, McCoy A, McNicholas SJ, Murshudov GN, Pannu NS, Potterton EA, Powell HR, Read RJ, Vagin A, Wilson KS. 2011. Overview of the CCP4 suite and current developments. *Acta Crystallographica. Section D, Biological Crystallography* **67**:235–242. DOI: https://doi.org/10.1107/S0907444910045749, PMID: 21460441

Xu Z, Kohli E, Devlin KI, Bold M, Nix JC, Misra S. 2008. Interactions between the quality control ubiquitin ligase CHIP and ubiquitin conjugating enzymes. *BMC Structural Biology* **8**:26. DOI: https://doi.org/10.1186/1472-6807-8-26, PMID: 18485199

Zhang YE. 2009. Non-Smad pathways in TGF-beta signaling. *Cell Research* **19**:128–139. DOI: https://doi.org/10.1038/cr.2008.328, PMID: 19114990

Zheng N, Wang P, Jeffrey PD, Pavletich NP. 2000. Structure of a c-Cbl-UbcH7 complex: RING domain function in ubiquitin-protein ligases. *Cell* **102**:533–539. DOI: https://doi.org/10.1016/s0092-8674(00)00057-x, PMID: 10966114

Zheng N, Shabek N. 2017. Ubiquitin ligases: structure, function, and regulation. *Annual Review of Biochemistry* **86**:129–157. DOI: https://doi.org/10.1146/annurev-biochem-060815-014922, PMID: 28375744